iScience

CellPress
OPEN ACCESS

Article

Diffusion of activated ATM explains γH2AX and MDC1 spread beyond the DNA damage site

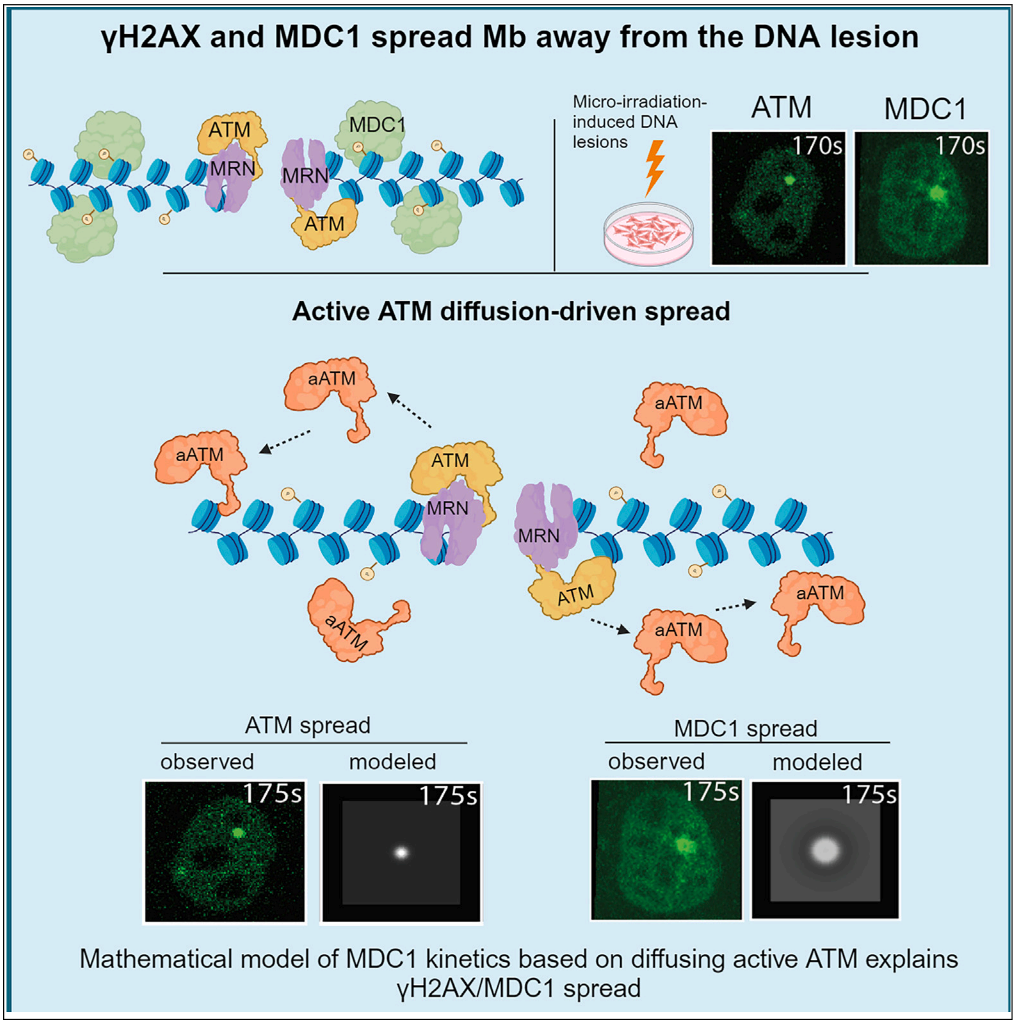

Georgi Danovski, Greta Panova, Bradley Keister, ..., Radoslav Aleksandrov, Krastan B. Blagoev, Stoyno S. Stoynov

stoynov@bio21.bas.bg

Highlights

Loop extrusion machinery accumulates before the MDC1 spread beyond DNA lesions

Cohesin is not required for the γH2AX/MDC1 spread at DSBs and complex lesions

Mathematical models were devised to describe ATM and MDC1 dynamics at DNA lesions

Free diffusion of activated ATM beyond the damage site explains γH2AX/MDC1 spread

Danovski et al., iScience 27, 110826
September 20, 2024
https://doi.org/10.1016/j.isci.2024.110826

iScience

CellPress
OPEN ACCESS

Article

Diffusion of activated ATM explains γH2AX and MDC1 spread beyond the DNA damage site

Georgi Danovski,[1] Greta Panova,[2] Bradley Keister,[3] Georgi Georgiev,[4] Aleksandar Atemin,[1] Sonya Uzunova,[1] Rumen Stamatov,[1] Petar-Bogomil Kanev,[1] Radoslav Aleksandrov,[1] Krastan B. Blagoev,[1,5,6,7] and Stoyno S. Stoynov[1,8,*]

SUMMARY

During DNA repair, ATM-induced H2AX histone phosphorylation and MDC1 recruitment spread megabases beyond the damage site. While loop extrusion has been suggested to drive this spread, the underlying mechanism remains unclear. Herein, we provide two lines of evidence that loop extrusion is not the only driver of damage-induced γH2AX spread. First, cohesin loader NIPBL and cohesin subunit RAD21 accumulate considerably later than the phosphorylation of H2AX and MDC1 recruitment at micro-IR-induced damage. Second, auxin-induced RAD21 depletion does not affect γH2AX/MDC1 spread following micro-irradiation or DSB induction by zeocin. To determine if diffusion of activated ATM could account for the observed behavior, we measured the exchange rate and diffusion constants of ATM and MDC1 within damaged and unperturbed chromatin. Using these measurements, we introduced a quantitative model in which the freely diffusing activated ATM phosphorylates H2AX. This model faithfully describes the dynamics of ATM and subsequent γH2AX/MDC1 spread at complex DNA lesions.

INTRODUCTION

A comprehensive understanding of the DNA damage response and its involvement in the maintenance of the genomic stability and prevention of carcinogenesis,[1–3] would require not only knowledge of the proteins involved and their interactions,[4–6] but also of their spatiotemporal dynamics within the cell.[7] To this end, one needs precise measurements and modeling of repair factor kinetics. We and others have measured the kinetics of recruitment and release of repair factors at DNA damage sites, an approach that allows us to obtain a detailed quantitative understanding of DNA repair mechanisms through the mathematical modeling of the physical processes taking place.[8,9]

A key event during the repair of DNA double-strand breaks (DSB) is the phosphorylation of the histone H2AX on serine 139 (γH2AX)[10–13] by the ataxia telangiectasia modified (ATM) protein kinase. The H2AX variant can account for up to 25% of the H2A pool, which allows a relative abundance of γH2AX around DSBs.[12] This modification is subsequently recognized by the mediator of DNA damage checkpoint protein 1 (MDC1).[14–17] While ATM and the MRN complex, which recruits the former, both localize to the DNA damage site, γH2AX spreads out over several megabases of DNA beyond the damage site.

Multiple studies have proposed that DNA damage-induced γH2AX spread is considerably influenced by 3D chromatin structure. Natale et al.[18] reported that individual large repair protein foci consist of several nano-foci organized in clusters around a DSB. These clusters were suggested to depend on chromatin architecture and CTCF. Using 4C-seq, which provides a high-resolution map of chromatin contacts, it was found that the spatial distribution of γH2AX is correlated with the chromatin contacts near DSBs.[19] Based on differential 4C-seq, Arnould et al.[20,21] proposed loop extrusion as a major determinant of γH2AX distribution. That is, cohesin-dependent loop extrusion at the DSB drives ATM-mediated H2AX phosphorylation at the megabase scale. Despite extensive studies into the matter, the exact mechanism through which the H2AX phosphorylation and downstream MDC1 recruitment spread beyond the repair site remains unclear.

To gain insight into the mechanism of γH2AX spread, we measured the spatiotemporal kinetics of proteins involved in this process at sites of micro-irradiation (micro-IR)-induced complex DNA lesions. We found that MDC1 is recruited faster than cohesin loader NIPBL and cohesin subunit RAD21 at damage sites, which suggests that mechanisms other than loop extrusion may also contribute to γH2AX spread. In fact, RAD21 depletion had no effect on γH2AX spread at micro-IR- and zeocin-lesions. Precise measurements of ATM and MDC1 recruitment

---

[1]Institute of Molecular Biology, Bulgarian Academy of Sciences, 21, G. Bontchev Str, 1113 Sofia, Bulgaria
[2]Department of Mathematics, USC, CA 90089, USA
[3]Department of Physics, UCSD, CA 92093, USA
[4]Faculty of Mathematics and Informatics, Sofia University, St. Kliment Ohridski, 5 James Bourchier Boulevard, 1164 Sofia, Bulgaria
[5]National Science Foundation, Alexandria, VA 22230, USA
[6]Department of Biophysics, Johns Hopkins University, Baltimore, MD 21218, USA
[7]Institut Curie, PSL Research University, Sorbonne Université, CNRS UMR3664, Paris, France
[8]Lead contact
*Correspondence: stoynov@bio21.bas.bg
https://doi.org/10.1016/j.isci.2024.110826

iScience *27*, 110826, September 20, 2024 © 2024 The Author(s). Published by Elsevier Inc.

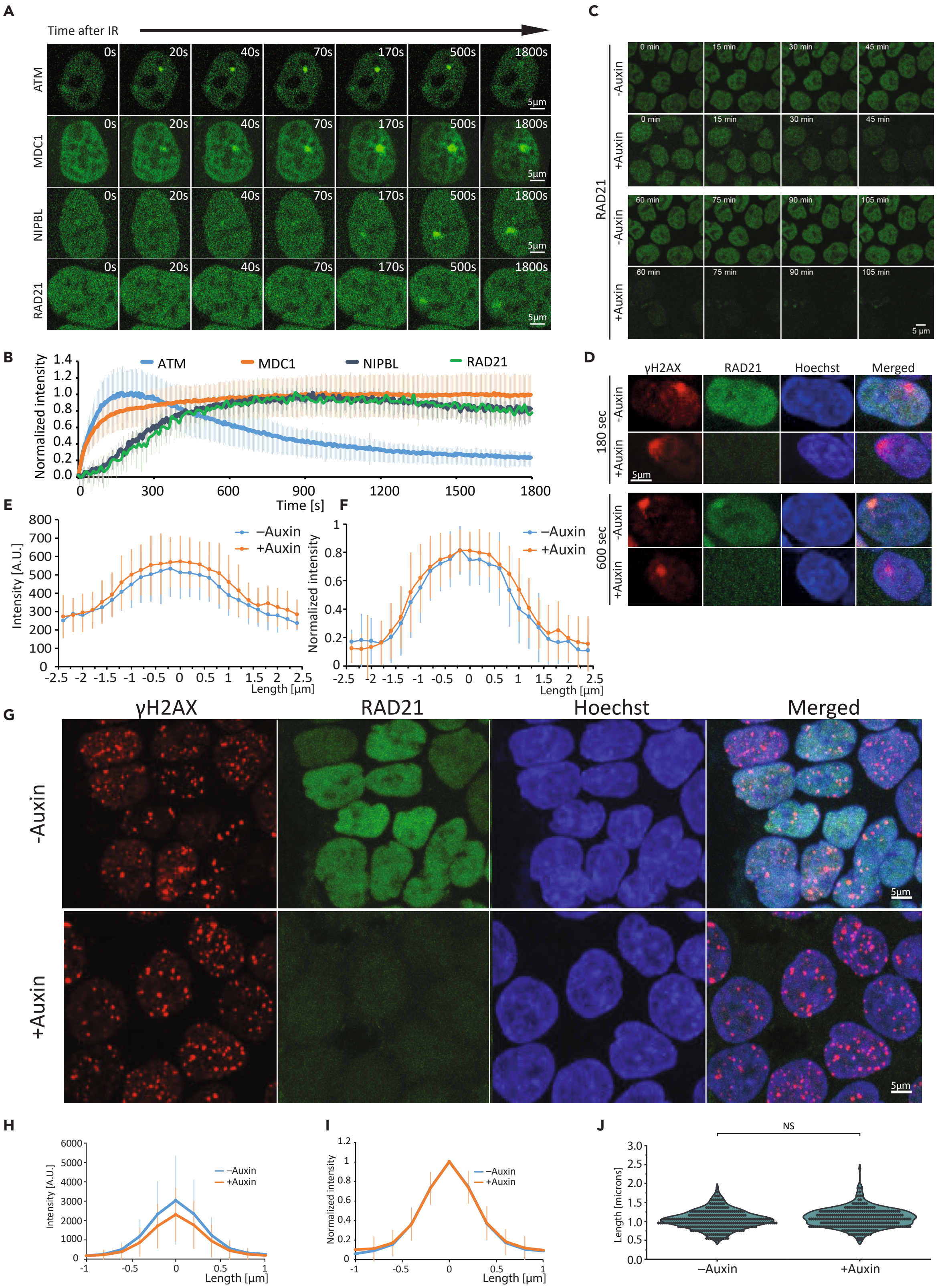
A
Time after IR
0s
20s
40s
70s
170s
500s
1800s
ATM
MDC1
NIPBL
RAD21
5µm
C
RAD21
-Auxin
+Auxin
0 min
15 min
30 min
45 min
60 min
75 min
90 min
105 min
5 µm
B
Normalized intensity
1.4
1.2
1.0
0.8
0.6
0.4
0.2
0.0
ATM
MDC1
NIPBL
RAD21
0
300
600
900
1200
1500
1800
Time [s]
D
γH2AX
RAD21
Hoechst
Merged
180 sec
600 sec
-Auxin
+Auxin
5µm
E
Intensity [A.U.]
800
700
600
500
400
300
200
100
0
−Auxin
+Auxin
-2.5 -2 -1.5 -1 -0.5 0 0.5 1 1.5 2 2.5
Length [µm]
F
Normalized intensity
1
0.8
0.6
0.4
0.2
0
−Auxin
+Auxin
-2.5 -2 -1.5 -1 -0.5 0 0.5 1 1.5 2 2.5
Length [µm]
G
γH2AX
RAD21
Hoechst
Merged
-Auxin
+Auxin
5µm
H
Intensity [A.U.]
6000
5000
4000
3000
2000
1000
0
−Auxin
+Auxin
-1 -0.5 0 0.5 1
Length [µm]
I
Normalized intensity
1.2
1
0.8
0.6
0.4
0.2
0
−Auxin
+Auxin
-1 -0.5 0 0.5 1
Length [µm]
J
NS
Length [microns]
3.0
2.5
2.0
1.5
1.0
0.5
0.0
−Auxin
+Auxin

Figure 1. Spatiotemporal dynamics of ATM, MDC1, mNIPBL, γH2AX, and RAD21 at sites of complex DNA damage

(A) Representative time-lapse microscopy images of the spatial distribution of ATM, MDC1, mNIPBL, and RAD21 at a micro-IR-induced complex DNA lesion. Scale bar: 5 μm. All time points can be observed in Videos S1 and S3.

(B) ATM (*N* = 17 foci), MDC1 (*N* = 57 foci), mNIPBL (*N* = 30 foci), and RAD21 (*N* = 12 foci) recruitment kinetics at the sites of complex DNA damage (error bars show the standard deviation). Data are presented as the mean ± standard deviation (SD).

(C) Time-lapse imaging of auxin-induced RAD21 degradation in HCT116 cells. Scale bar: 5 μm.

(D) Representative immunofluorescence images of γH2AX and RAD21 in cells subjected to micro-IR, with or without auxin-induced RAD21 degradation. Scale bar: 5 μm.

(E) Intensity profile across the major axis of micro-IR-induced γH2AX foci, with (*N* = 42 foci) or without (*N* = 34 foci) auxin-induced RAD21 degradation. Data are presented as the mean ± SD.

(F) Normalized intensity profile across the major axis of micro-IR-induced γH2AX foci, with (*N* = 42 foci) or without (*N* = 34 foci) auxin-induced RAD21 degradation. Data are presented as the mean ± SD.

(G) Representative immunofluorescence images of γH2AX and RAD21 in zeocin-treated cells, with or without auxin-induced RAD21 degradation. Scale bar: 5 μm.

(H) Intensity profile across γH2AX foci in zeocin-treated cells, with or without auxin-induced RAD21 degradation. Data are presented as the mean ± SD. *N* = 300 foci per condition.

(I) Normalized intensity profile across the major axis of γH2AX foci in zeocin-treated cells, with or without auxin-induced RAD21 degradation. Data are presented as the mean ± SD. *N* = 300 foci per condition.

(J) Distribution of γH2AX foci major axis length in zeocin-treated cells, with and without auxin-induced RAD21 degradation. Data were analyzed via the unpaired t-test and are presented as the mean ± SD. NS = not significant, significance level: *p* = 0.01. *N* = 300 foci per condition.

and exchange kinetics, together with the data on their spatiotemporal concentrations, allowed us to test several reaction-diffusion mathematical models[22] describing the kinetics of γH2AX/MDC1 spread. Our results demonstrate that activated ATM diffusing away from the damage site can explain the observed spatiotemporal distribution of MDC1 at complex DNA lesions.

RESULTS

Dynamics of MDC1 at complex DNA lesions

To follow H2AX phosphorylation in space and time in living cells, we measured the kinetics of MDC1 at a complex DNA lesion, generated through micro-IR within a small, localized three-dimensional region. To this end, we used an EGFP-tagged MDC1 transgenic HeLa Kyoto cell line,[23] generated through bacterial artificial chromosome (BAC) recombination.[24] In this line, the tagged MDC1 is expressed at near-physiological levels[25] under cell-cycle control. Our results (Figures 1A and 1B; Video S1) show that MDC1 is quickly recruited to the site of micro-IR,[8,26] with a half-time of 55s, reaching its maximum levels at around 900s, whereafter it spreads around the complex lesion. As a result, MDC1 is heavily depleted from other regions of the nucleus following damage induction. Comparing the kinetics of MDC1 recruitment and depletion, we see a significant delay in the latter process, which could be attributed to the slower diffusion of MDC1 within the nucleus.

To confirm whether this was the case, we performed FRAP of a small region within the nucleus in the absence of damage. The diffusion calculated based on MDC1-EGFP signal recovery after photobleaching (Figure S1) was approximately an order of magnitude slower (average D = 0.055 ± 0.033 $\mu m^2/s$) than expected for the pure diffusion of a 200-kDa (0.4–0.6 $\mu m^2/s$) protein. This observation is in line with the previously reported weak interaction of MDC1 with chromatin in the absence of DNA damage.[26,27] Such an association of MDC1 with chromatin, in the absence of a lesion, could explain its slower effective diffusion. To quantify the effect of complex DNA damage on MDC1 chromatin residence, we followed the recovery of micro-IR-induced MDC1 foci after photobleaching, observing an even slower exchange (27.5 ± 11s) compared to that at unperturbed chromatin (Figures S1A and S1B; Video S2).

Apart from ATM, ATR and DNA-PK are also known to phosphorylate H2AX in response to DNA damage. However, neither of the two was shown to directly contribute to the γH2AX spread phenomenon. DNA-PK binds Ku70/80 at DSB ends, phosphorylating H2AX exclusively at the break. ATR is recruited to RPA-coated ssDNA via its interaction partner ATRIP and phosphorylates H2AX in proximity.[20,28] Indeed, co-inhibition of ATR and DNA-PK had no effect on γH2AX spread and concentration but did result in a slight delay of MDC1 recruitment to micro-IR-induced complex lesions (Figures S1D and S1E). This could be attributed to the lack of DNA-PK-dependent H2AX phosphorylation, which takes place at an earlier timepoint after damage induction since DNA-PK is recruited before ATM.[8]

Chromatin binding affects MDC1 mobilization to a secondary damage site

Exposure to genotoxins (e.g., radiation, chemotherapy, and radiomimetics) induces more than a single lesion. We reasoned that the slow mobility of MDC1 may have an impact on DNA repair at multiple damage sites. To interrogate this, we induced a second lesion at a distant nuclear locus 30 min after the initial micro-IR insult. Formation of the second MDC1 damage focus led to a decrease in the amount of MDC1 at the first one (Figures 2A and 2B). However, the kinetics of MDC1 removal at the first focus was significantly slower than that of its recruitment at the second lesion. These results demonstrate that the slow intranuclear transport of MDC1 due to chromatin binding influences the kinetics and spread of MDC1 following the consecutive induction of two complex lesions.

ATM is rapidly exchanged at complex DNA lesions

To better understand MDC1 spread kinetics, we also measured the kinetics of ATM, the major apical kinase responsible for H2AX phosphorylation at DNA damage sites. ATM is recruited earlier (half-time of recruitment: 40s) than MDC1[8] and, in contrast to the latter, accumulates

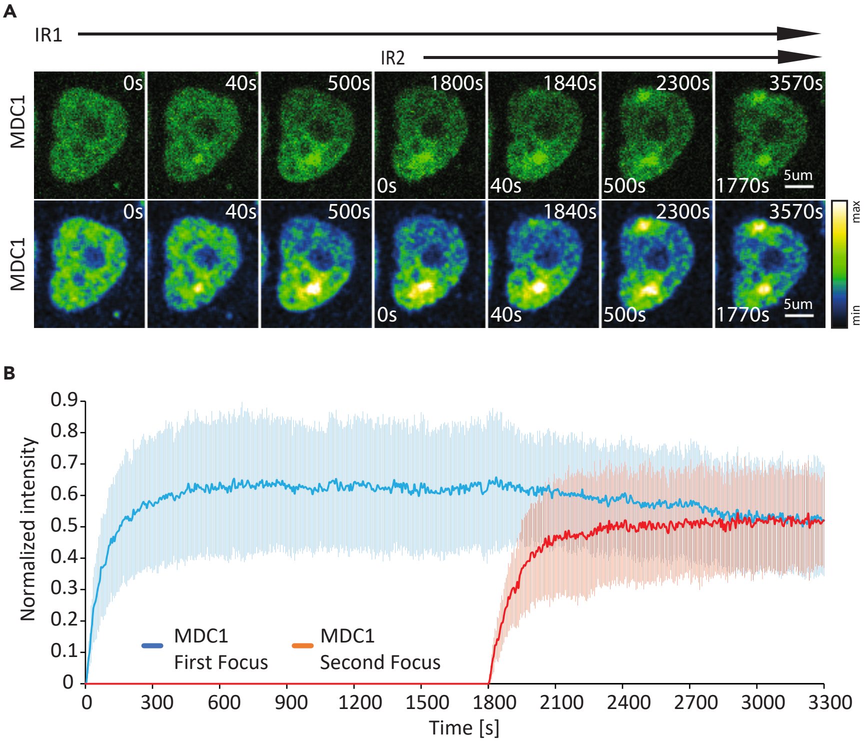

Figure 2. MDC1 recruitment kinetics at two consecutive micro-irradiation-induced complex DNA lesions

(A) Representative time-lapse images are presented in the row above. The row below presents the same images where intensity is color coded. Scale bar: 5 μm.

(B) Recruitment kinetics of consecutive micro-irradiation-induced MDC1 foci. Data are presented as the mean ± SD. *N* = 19 pairs of foci.

only within the DNA damage site (Figures 1A and 1B; Video S1). ATM rapidly accumulates upon micro-IR (reaching a maximum after 210s), which is followed by a rapid decrease shortly thereafter (Figure 1B). The transition between ATM accumulation confined within the damaged region and the subsequent expansion, or spread, of γH2AX and MDC1 remains mechanistically undetermined.

Arnould et al. put forth a model wherein activated ATM is localized to the boundaries of cohesin-dependent chromatin loops next to a DSB.[20] Subsequently accumulated repair machinery prevents loop extrusion in one direction, while extrusion proceeds in the other, with ATM phosphorylating the chromatin pulled through to spread γH2AX. ATM binding and phosphorylation while DNA is being pulled through suggests a rather slow ATM exchange. However, our FRAP measurements at micro-IR-induced complex lesions revealed very fast ATM exchange rates[29] (Figures S1A and S1B), close to those of freely diffusing ATM (Figure S1C).

RAD21 degradation does not limit γH2AX/MDC1 spread

To understand the timescale at which loop extrusion operates and thus validate the above-described model, we compared the accumulation rate of cohesin loader NIPBL, which is required for DSB-dependent cohesin recruitment and loop extrusion, with those of ATM and MDC1 (Figures 1A and 1B; Video S1). This comparison revealed that MDC1 and ATM were recruited considerably faster than mouse NIPBL (mNIPBL), which suggests that the MDC1 spread occurs before DSB-induced loop extrusion. This is also supported by the finding that MDC1 and RNF168 are required for mNIPBL loading.[30] To directly confirm cohesin recruitment timing, we employed cells expressing endogenously tagged cohesin subunit RAD21, which exhibit comparable loop extrusion activity to wild-type cells.[31,32] RAD21 recruitment kinetics closely followed those of mNIPBL, being significantly slower than MDC1 (Figures 1A and 1B; Video S3).

To assess if loop extrusion machinery loaded prior to damage induction drives γH2AX/MDC1 spread, we employed auxin-inducible degradation to deplete RAD21 endogenously tagged with mClover and an auxin-inducible degron (AID). As previously established,[31,32] treatment with auxin resulted in the complete depletion of RAD21-mClover-AID by 90 min (Figure 1C) and loss of loop extrusion activity.[31,32] To determine the effect of RAD21 depletion on γH2AX distribution at the sites of DNA lesions, we fixed cells 120 and 600 s after micro-IR. γH2AX immunofluorescence staining revealed comparably spread foci with or without RAD21 degradation (Figure 1D), which was confirmed by the quantification of the fluorescence intensity profiles across the major axis of foci (Figures 1E and 1F). These results suggest that RAD21-mediated loop extrusion is not the sole driver of γH2AX spread at the sites of complex DNA lesions. At 120 s, γH2AX spread, but not RAD21 recruitment was observed in cells where RAD21 degradation was not induced. In line with our live-cell imaging data, RAD21 accumulation was detected at 600 s. These results confirmed that, as shown for MDC1, γH2AX spread also precedes the recruitment of loop extrusion machinery. To exclude a scenario where loop extrusion drives γH2AX spread exclusively at DSBs, we treated cells with the DSB-inducing agent zeocin

(Figure 1G). RAD21 depletion had no effect on the intensity profile of γH2AX foci in zeocin-treated cells (Figures 1G–1I). Furthermore, there was no significant difference in foci size, as inferred based on major axis length ($p = 0.0525$) (Figure 1J). Taken together, our results indicate that mechanisms other than loop extrusion also contribute to γH2AX/MDC1 spread at DNA lesions.

An additional mechanism promoting γH2AX/MDC1 spread away from the micro-IR-induced DNA lesions could occur through diffusing activated ATM, which phosphorylates chromatin along its path. In this model, ATM binds at the damage site, is activated, and then released. Upon its detachment from the damage site, freely diffusing activated ATM phosphorylates the γH2AX along its path until inactivated. We introduced multiple quantitative mathematical models to describe this phosphorylation mechanism and confirm whether they are consistent with our measurements.

Modeling of MDC1 spread based on diffusing activated ataxia telangiectasia modified

The correct spatiotemporal mathematical model of MDC1 distribution should be able to quantitatively explain the kinetics of ATM and MDC1 recruitment and removal throughout the whole nucleus after the induction of complex DNA lesions. The model should also faithfully describe the actual heterogeneous chemical reaction parameters derived from FRAP of ATM and MDC1 at DNA damage sites.

The first model that we developed describes ATM and MDC1 data via the following reactions:

$$Z_0 \overset{k_0}{\rightarrow} X \tag{Equation 1}$$

$$ATM + X \underset{k_{off}}{\overset{k_{on}}{\rightleftharpoons}} ATMX \tag{Equation 2}$$

$$ATMX \underset{k_d}{\overset{k_3}{\rightleftharpoons}} \alpha ATMX \tag{Equation 3}$$

$$\alpha ATMX \overset{k_d}{\rightarrow} \alpha ATM + X_m \tag{Equation 4}$$

$$\alpha ATM \overset{k_d}{\rightarrow} ATM \tag{Equation 5}$$

$$H2AX \underset{k_{r_h}}{\overset{k_{f_h}(\alpha ATM+\alpha ATMX)}{\rightleftharpoons}} \gamma H2AX \tag{Equation 6}$$

$$\gamma H2AX + MDC1 \underset{k_{offMDC}}{\overset{k_{onMDC}}{\rightleftharpoons}} \gamma H2AXMDC1 \tag{Equation 7}$$

Here, Z_0 represents the DNA damage, and X represents the proteins bound to damage sites, e.g., the MRN complex, which accumulates prior to ATM recruitment. ATMX represents the bound ATM, αATM is the activated ATM, αATMX represents the bound αATM and mX represents modified X after αATM removal. The partial differential equations describing these kinetic reactions for the corresponding concentrations are provided in the supplementary information (Data S1). We will call this model the "Standard αATM diffusion model," or the "Standard model," for simplicity (Figure 3). This model describes the DNA damage within the irradiated region of the nucleus, which is converted into a DNA damage-protein complex before the ATM binding, with a rate k_1. ATM binds and unbinds to this complex with rates k_{on} and k_{off}, respectively. ATM undergoes reversible activation at the damage site, whereafter activated ATM leaves the site irreversibly, with a rate k_4. Consequently, the now freely diffusing activated ATM is deactivated with the same rate constant as the bound activated ATM. Once activated, both the bound and unbound αATM phosphorylate H2AX to γH2AX with a rate k_f, which depends on the αATM concentration. Phosphorylated H2AX is then recognized by MDC1, forming a γH2AX/MDC1 complex.

We model the biological processes shown in reactions (1–7) by including the diffusion of molecules through a system of reaction-diffusion partial differential equations for the corresponding concentrations. The reaction-diffusion equations that correspond to these reactions and the details of our numerical implementation are shown in the Supplementary information (Data S1). We created a dedicated software tool (BioModelSolver) in order to simulate ATM and MDC1 nuclear dynamics following micro-IR as per an assigned model. BioModelSolver enabled us to generate time-lapse images of the modeled process, in addition to two graphical representations. The first follows protein-of-interest concentration in a given nuclear region over time. The latter representation visualizes the spatial distribution of protein concentration within a given region as a time-lapse video. This tool enabled to the comparison of experimental data against model predictions.

Using live-cell microscopy, we were able to measure several physical parameters that were implemented in the mathematical model (Table S1). The ATM diffusion constant was measured using FRAP of the unbound ATM (average $D = 0.664 \pm 0.34\ \mu m^2/s$). Complex MDC1 transport was modeled with an effective diffusion constant, which we also measured using FRAP of cells without DNA damage (average $D = 0.055 \pm 0.35\ \mu m^2/s$). This effective diffusion constant captures the free diffusion as well as the process of MDC1 binding and unbinding to

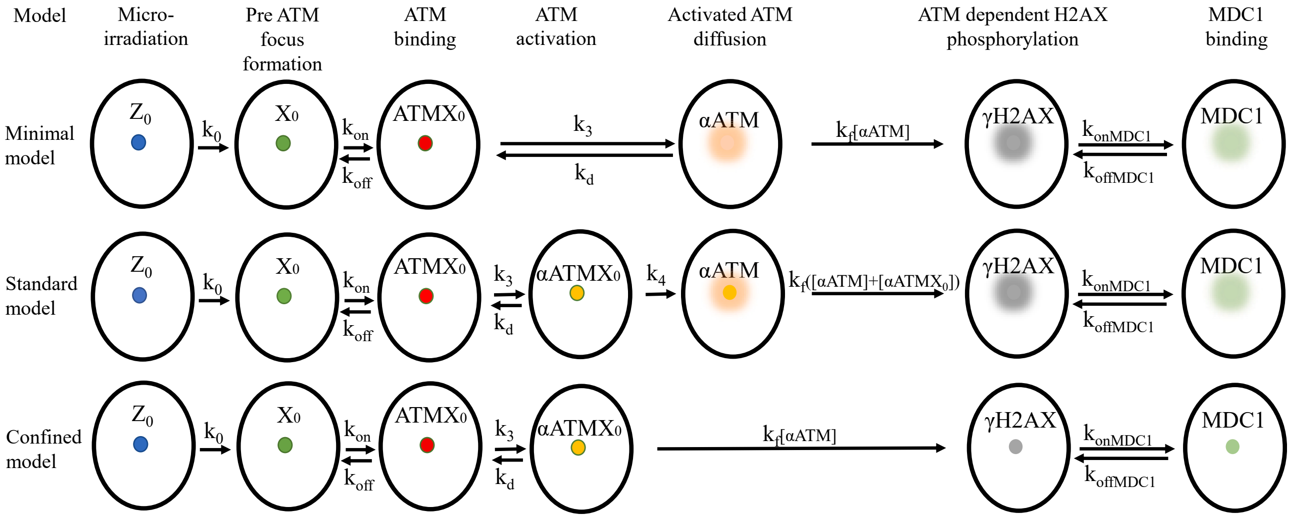

Figure 3. Graphical representation of the three mathematical models describing the ATM-dependent H2AX phosphorylation and MDC1 recruitment dynamics

the undamaged chromatin. Other input parameters the ATM and MDC1 concentrations were calculated (material and methods) using their cell copy numbers, obtained.[25] We measured the time course of ATM and MDC1 fluorescence intensity at the DNA damage site as well as in a small region of interest outside this site. MDC1 spatial distribution around the damage site was also obtained. Using the initial ATM and MDC1 concentrations in the nucleus allowed us to convert the fluorescence intensity to concentrations.

To obtain the kinetic rates of reactions (1–9), we fit the standard model to our experimental data, which include: (1) the concentrations of MDC1 (Figures 4A and 4C) and ATM (Figures 5A and 5C) at the damage site as well as in a nuclear region away from it; (2) the concentrations of MDC1 (Figures 6A and 6B) and ATM (Figures 7A–7C) after FRAP of the damage site. Importantly, in order to assess whether the proposed models can explain the observed pattern of MDC1 spread, we compare the measured spatial distribution of MDC1 (Figures 4B and S2; Video S4) and ATM (Figures 5B and S3; Video S5) around micro-IR-induced damage foci over time versus those predicted by the model.

We were able to find a set of parameters (Table S1) that fit the numerical solutions of the reaction-diffusion equations to the experimental data (see STAR Methods). We provide graphical representations of the proposed numerical solutions for MDC1 (Figure 4C) and ATM (Figure 5C) recruitment as well as for their depletion in the nuclear region away from the damage site.

The standard model (1–9) accurately fit the measured MDC1 (Figure 4C) and ATM (Figure 5C) recruitment kinetics and quantity at the site of DNA damage as well as the simultaneous depletion of the given protein in a nuclear region away from the damage site. Furthermore, the model accurately predicted the spatiotemporal distribution of ATM (Figures 5B and S3; Video S5) and MDC1 (Figures 4B and S2; Video S4), in particular the spread of the latter away from the damage site (Figure S4; Video S6). The model also accurately fits the measured MDC1 (Figure 6B) and ATM (Figures 7B and 7C) exchange rates at the site of DNA damage (determined via FRAP).

A particularly impressive feature of such modeling is that it can recapitulate complex kinetics which include ATM recruitment and removal after damage induction, followed by FRAP at the damage site (Figure S5).

From fitting the model to the data, we found that the αATM effective diffusion coefficient (average $D = 0.059\ \mu m^2/s$) should be 10 times smaller than the diffusion coefficient of the non-activated ATM (Table S1). A possible reason for the slow diffusion of αATM is that its transport involves multiple rounds of binding to, phosphorylation of, and unbinding from the H2AX anchored within chromatin as well as its free diffusion in between these events. The magnitude of the effective diffusion coefficient is similar to the diffusion coefficient of MDC1. The delay in MDC1 depletion from outside of the DNA damage shown in Figure 4C and the area to which MDC1 spreads are very sensitive to the value of MDC1 and αATM diffusion coefficients, which highlights the importance of their diffusion for the MDC1 spread kinetics. The standard model also implies that the concentration of lesion-bound and freely diffusing αATM are two orders of magnitude lower than that of total bound inactive ATM at the damage site (Figure S6; Video S7).

Minimal model explaining MDC1 spread based on diffusing activated ATM

Interestingly, the goodness of fit was not affected by changes in k_4 (Table S1), a rate constant describing the dissociation of αATM from the damage site (Equation 4). The MDC1 spread could therefore be explained without the presence of bound αATM at the site of damage. Rather, this model postulates that ATM is immediately released upon its activation. We will call this model the "Minimal αATM diffusion model," or the "Minimal model," for simplicity. Here, reactions (3) and (4) from the first model are replaced by (10). The best Minimal model fit of the experimental MDC1 (Figures 4A, 4E, 4D and S2; Video S4) and ATM (Figures 5A, 5E, 5D and S3; Video S5) data was as accurate as that of the Standard model, including for MDC1/ATM spatial distribution (Figure S4; Video S6) and MDC1/ATM FRAP data (Figures 6C; 7D and 7F).

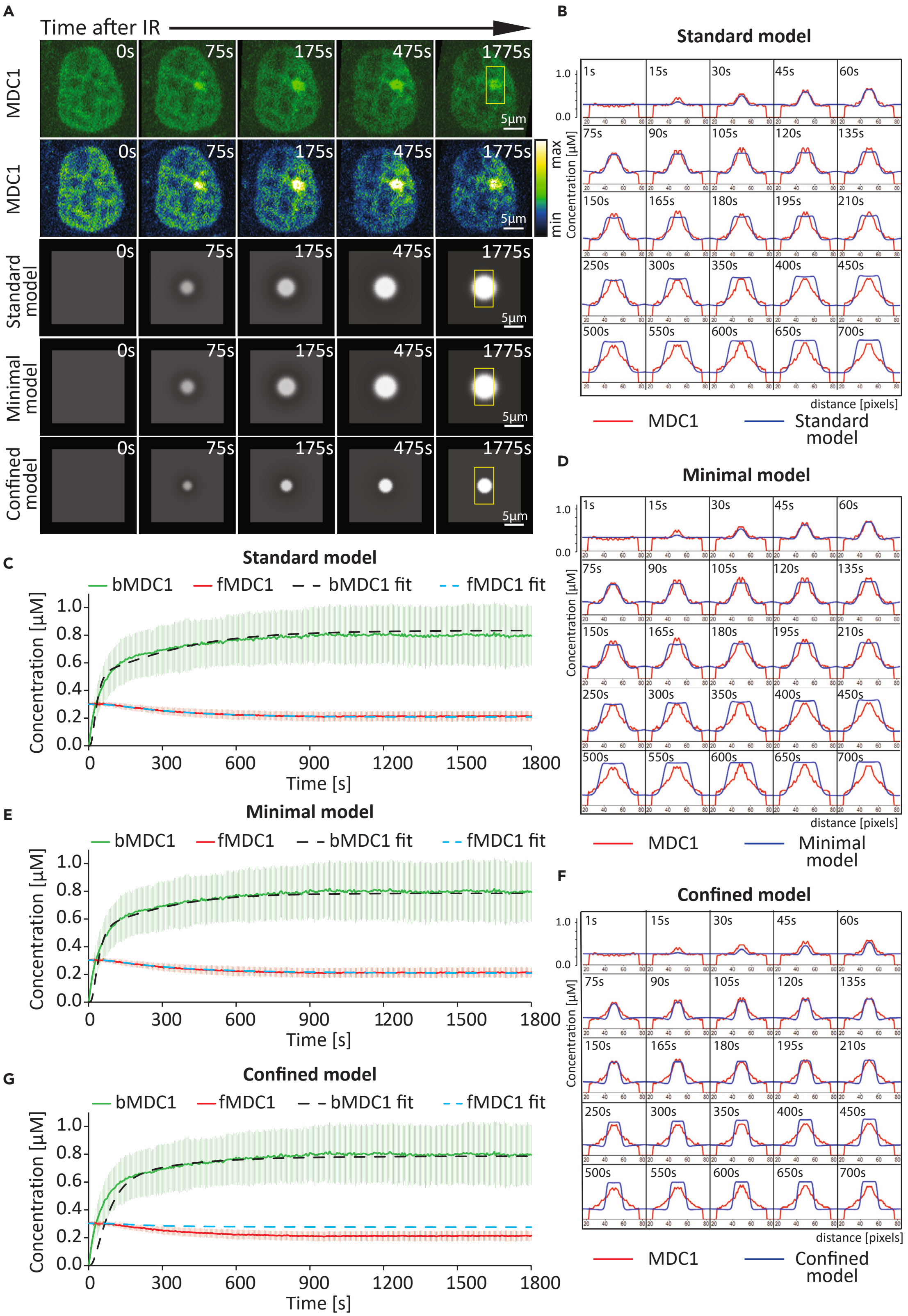
A
Time after IR
MDC1
MDC1
Standard model
Minimal model
Confined model
0s
75s
175s
475s
1775s
5μm
max
min
B
Standard model
1.0
0.0
Concentration [μM]
1s
15s
30s
45s
60s
75s
90s
105s
120s
135s
150s
165s
180s
195s
210s
250s
300s
350s
400s
450s
500s
550s
600s
650s
700s
20
40
60
80
distance [pixels]
MDC1
Standard model
C
Standard model
bMDC1
fMDC1
bMDC1 fit
fMDC1 fit
Concentration [μM]
1.0
0.8
0.6
0.4
0.2
0.0
0
300
600
900
1200
1500
1800
Time [s]
D
Minimal model
MDC1
Minimal model
E
Minimal model
F
Confined model
MDC1
Confined model
G
Confined model

Figure 4. Comparison between the experimentally measured and predicted MDC1 dynamics at sites of complex DNA damage

(A) Comparison between time-lapse microscopy images and images generated via simulation based on the models of MDC1 distribution at sites of complex DNA damage. The yellow box covers a region of interest where the MDC1 spread presented in B, D, and F is measured. Scale bar: 5 μm.

(B) Time-lapse representation of the MDC1 concentration profile across the micro-irradiation site (the region of interest in A). Red color indicates the measured MDC1 concentration spread. Blue indicates the best-fitting predicted concentration based on the standard model.

(C) Graphical comparison between the experimentally measured MDC1 dynamics (*N* = 57 foci) at sites of complex DNA damage and those predicted based on the standard model. Data are presented as mean ± SD. bMDC1 (bound MDC1), measured concentration (μM) of MDC1 within the DNA damage site; fMDC1 (free MDC1), measured concentration (μM) of MDC1 outside of the damage focus; bMDC1 fit, the best-fitting predicted concentration (μM) of MDC1 at the damage site, based on the standard model; fMDC1 fit, the best-fitting predicted concentration (μM) of MDC1 outside of the damage site, based on the standard model.

(D) Time-lapse representation of the MDC1 concentration profile across the micro-irradiation site (the region of interest in A). Red color indicates the measured MDC1 concentration spread. Blue indicates the best-fitting predicted concentration based on the minimal model.

(E) Graphical comparison between the experimentally measured MDC1 dynamics (*N* = 57 foci) at sites of complex DNA damage and those predicted based on the minimal model. Data are presented as mean ± SD. bMDC1, measured concentration (μM) of MDC1 within the DNA damage site; fMDC1, measured concentration (μM) of MDC1 outside of the damage focus; bMDC1 fit, the best-fitting predicted concentration (μM) of MDC1 at the damage site, based on the minimal model; fMDC1 fit, the best-fitting predicted concentration (μM) of MDC1 outside of the damage site, based on the minimal model.

(F) Time-lapse representation of the MDC1 concentration profile across the micro-irradiation site (the region of interest in A). Red color indicates the measured MDC1 concentration spread. Blue indicates the best-fitting predicted concentration based on the confined model.

(G) Graphical comparison between the experimentally measured MDC1 dynamics (*N* = 57 foci) at sites of complex DNA damage and those predicted based on the confined model. Data are presented as mean ± SD. bMDC1, measured concentration (μM) of MDC1 within the DNA damage site; fMDC1, measured concentration (μM) of MDC1 outside of the damage focus; bMDC1 fit, the best-fitting predicted concentration (μM) of MDC1 at the damage site, based on the confined model; fMDC1 fit, the best-fitting predicted concentration (μM) of MDC1 outside of the damage site, based on the confined model.

$$Z_0 \xrightarrow{k_0} X \qquad \text{(Equation 8)}$$

$$ATM + X \underset{k_{off}}{\overset{k_{on}}{\rightleftharpoons}} ATMX \qquad \text{(Equation 9)}$$

$$ATMX \underset{k_d}{\overset{k_3}{\rightleftharpoons}} \alpha ATMX + X_m \qquad \text{(Equation 10)}$$

$$\alpha ATM \xrightarrow{k_d} ATM \qquad \text{(Equation 11)}$$

$$H2AX \underset{k_{r_h}}{\overset{k_{f_h(\alpha ATM)}}{\rightleftharpoons}} \gamma H2AX \qquad \text{(Equation 12)}$$

$$\gamma H2AX + \mathrm{MDC1} \underset{k_{offMDC}}{\overset{k_{onMDC}}{\rightleftharpoons}} \gamma H2AX\mathrm{MDC1} \qquad \text{(Equation 13)}$$

MDC1 spread cannot be explained without the diffusion of activated ATM

We also checked whether the data can be fitted to a model in which the ATM is only active when bound to the damage site. We will call this model the "Confined αATM model," or the "Confined model," for simplicity. The Confined model is described by the following reactions:

$$Z_0 \xrightarrow{k_0} X \qquad \text{(Equation 14)}$$

$$ATM + X \underset{k_{off}}{\overset{k_{on}}{\rightleftharpoons}} ATMX \qquad \text{(Equation 15)}$$

$$ATMX \underset{k_d}{\overset{k_3}{\rightleftharpoons}} \alpha ATMX \qquad \text{(Equation 16)}$$

$$\alpha ATMX \xrightarrow{k_4} ATM + X_m \qquad \text{(Equation 17)}$$

$$H2AX \underset{k_{r_h}}{\overset{k_{f_{h(\alpha ATMX)}}}{\rightleftharpoons}} \gamma H2AX \qquad \text{(Equation 18)}$$

$$\gamma H2AX + \mathrm{MDC1} \underset{k_{offMDC}}{\overset{k_{onMDC}}{\rightleftharpoons}} \gamma H2AX\mathrm{MDC1} \qquad \text{(Equation 19)}$$

where reactions (4) and (5) from the original model are replaced by 17.

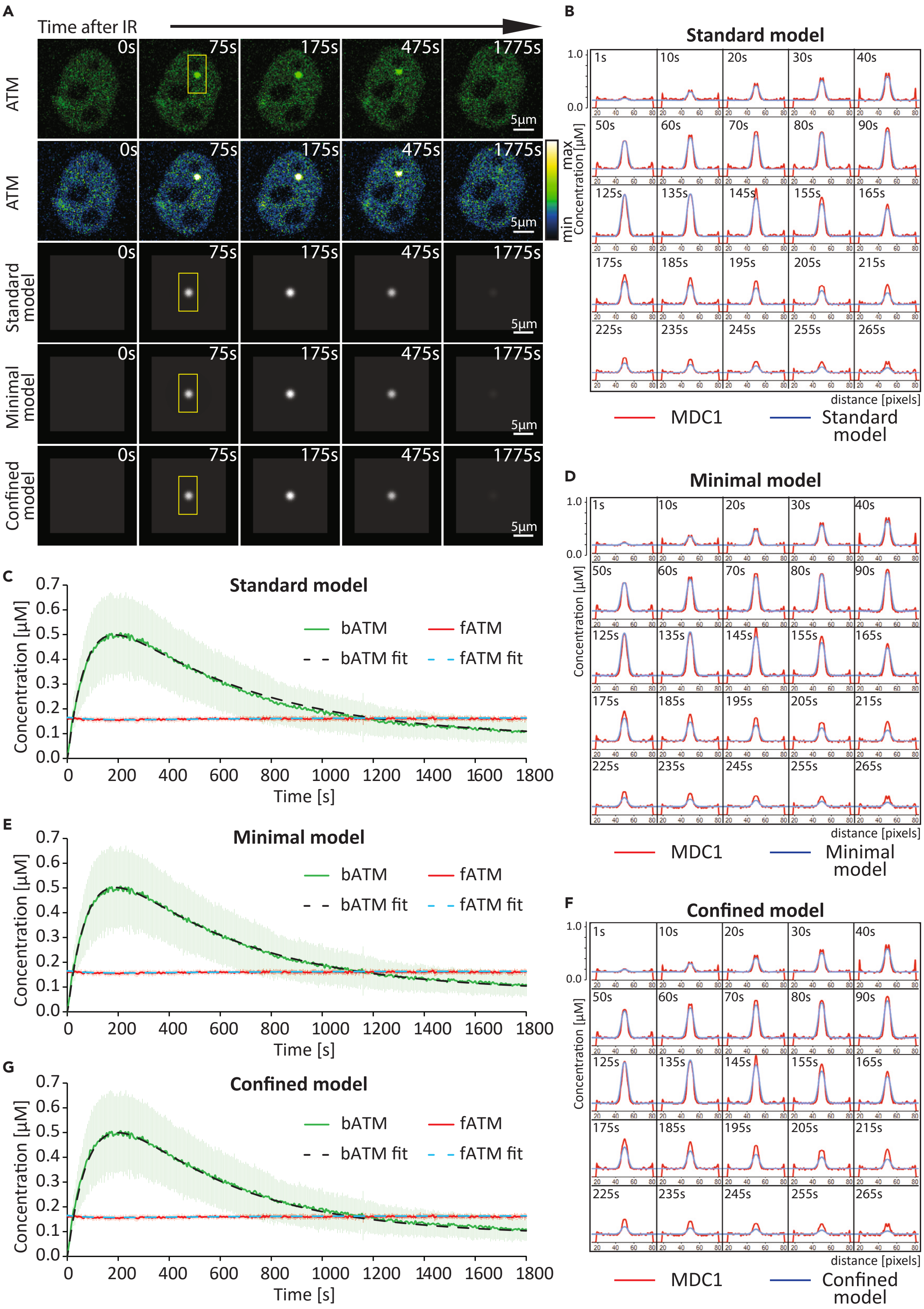
A
Time after IR
ATM
ATM
Standard model
Minimal model
Confined model
0s
75s
175s
475s
1775s
5µm
max
min
Concentration [µM]
B
Standard model
1.0
0.0
Concentration [µM]
1s 10s 20s 30s 40s
50s 60s 70s 80s 90s
125s 135s 145s 155s 165s
175s 185s 195s 205s 215s
225s 235s 245s 255s 265s
20 40 60 80
distance [pixels]
MDC1
Standard model
C
Standard model
Concentration [µM]
0.0 0.1 0.2 0.3 0.4 0.5 0.6 0.7
Time [s]
0 200 400 600 800 1000 1200 1400 1600 1800
bATM
fATM
bATM fit
fATM fit
D
Minimal model
1.0
0.0
Concentration [µM]
distance [pixels]
MDC1
Minimal model
E
Minimal model
Concentration [µM]
Time [s]
bATM
fATM
bATM fit
fATM fit
F
Confined model
1.0
0.0
Concentration [µM]
distance [pixels]
MDC1
Confined model
G
Confined model
Concentration [µM]
Time [s]
bATM
fATM
bATM fit
fATM fit

Figure 5. Comparison between the experimentally measured and predicted ATM dynamics at sites of complex DNA damage

(A) Comparison between time-lapse microscopy images and images generated via simulation based on the models of ATM distribution at sites of complex DNA damage. The yellow box covers a region of interest where the ATM spread presented in B, D, and F is measured. Scale bar: 5 μm.

(B) Time-lapse representation of the ATM concentration profile across the micro-irradiation site (the region of interest in A). Red color indicates the measured ATM concentration spread. Blue indicates the best-fitting predicted concentration based on the standard model.

(C) Graphical comparison between the experimentally measured ATM dynamics ($N = 17$ foci) at sites of complex DNA damage and those predicted based on the standard model. Data are presented as mean ± SD. bATM, measured concentration (μM) of ATM within the DNA damage site; fATM, measured concentration (μM) of ATM outside of the damage focus; bATM fit, the best-fitting predicted concentration (μM) of ATM at the damage site, based on the standard model; fATM fit, the best-fitting predicted concentration (μM) of ATM outside of the damage site, based on the standard model.

(D) Time-lapse representation of the ATM concentration profile across the micro-irradiation site (the region of interest in A). Red color indicates the measured ATM concentration spread. Blue indicates the best-fitting predicted concentration based on the minimal model.

(E) Graphical comparison between the experimentally measured ATM dynamics ($N = 17$ foci) at sites of complex DNA damage and those predicted based on the minimal model. Data are presented as mean ± SD. bATM, measured concentration (μM) of ATM within the DNA damage site; fATM, measured concentration (μM) of ATM outside of the damage focus; bATM fit, the best-fitting predicted concentration (μM) of ATM at the damage site, based on the minimal model; fATM fit, the best-fitting predicted concentration (μM) of ATM outside of the damage site, based on the minimal model.

(F) Time-lapse representation of the ATM concentration profile across the micro-irradiation site (the region of interest in A). Red color indicates the measured ATM concentration spread. Blue indicates the best-fitting predicted concentration based on the confined model.

(G) Graphical comparison between the experimentally measured ATM dynamics ($N = 17$ foci) at sites of complex DNA damage and those predicted based on the confined model. Data are presented as mean ± SD. bATM, measured concentration (μM) of ATM within the DNA damage site; fATM, measured concentration (μM) of ATM outside of the damage focus; bATM fit, the best-fitting predicted concentration (μM) of ATM at the damage site, based on the confined model; fATM fit, the best-fitting predicted concentration (μM) of ATM outside of the damage site, based on the confined model.

While this model fits the recruitment kinetics of ATM (Figures 5A, 5G, 5F, and S3; Video S5) at the DNA damage site well, it did not fit the early steps of MDC1 recruitment to the damage site nor its delayed depletion outside of the damage site (Figure 4G). Most importantly, the model could not recapitulate MDC1 spread beyond the micro-IR-induced complex lesion (Figures 4A, 4F, and S2; Videos S4 and S6). These observations suggest that αATM diffusion is critical for explaining MDC1 behavior during the repair of complex DNA lesions.

Altogether, our results demonstrate that cohesin-mediated loop extrusion is not the only mechanism responsible for the damage-induced spread of γH2AX and MDC1. To describe γH2AX/MDC1 spread, we introduce a mathematical theory that enables the spatiotemporal modeling of heterogeneous chemical reactions in cells. Through this mathematical description, we were able to demonstrate that the damage-induced spread of γH2AX and MDC1 can be explained by simple diffusion of activated ATM.

DISCUSSION

In the present work, to study the nature of γH2AX/MDC1 spread at complex DNA lesions, we followed the spatiotemporal dynamics of fluorescently tagged ATM, MDC1, NIPBL, and RAD21 through live-cell microscopy. Our measurements show that MDC1 transport in the absence of DNA damage is approximately an order of magnitude slower than expected from the pure diffusion of a similar-size protein, which is in line with a recent report demonstrating that most MDC1 molecules are indeed chromatin-bound in such conditions.[26,27] After irradiation, MDC1 was quickly recruited to the damage site and subsequently spread around the DNA lesion, being heavily depleted from other parts of the nucleus. The slow MDC1 transport and its limited concentration limit foci spread after sequential irradiation at two regions of interest. In contrast to MDC1, ATM is recruited at the site of DNA damage without spreading and exhibits a fast exchange rate, close to that of freely diffusing ATM.

We developed three quantitative models of ATM and MDC1 kinetics, two of which accurately fitted our imaging data. Critical for a successful fit was the inclusion of the diffusion of αATM outside of the damage site. In the simplest of these two models, ATM dissociates from the damage site upon its activation. While diffusing, it phosphorylates H2AX histones, and the spatial extent of the γH2AX and MDC1 spread is determined by the interplay between αATM effective diffusion and the rate of its deactivation. While the former leads to phosphorylation away from the focus, the distance to which phosphorylation extends is limited by the deactivation rate.

Our model of γH2AX/MDC1 spread based on αATM 3D diffusion explains a number of measurements and observations. First, it describes the spread rate and spatial concentration profile of MDC1, as well as its exchange and recruitment kinetics following UV laser micro-irradiation. Second, our model accurately predicts slow MDC1 transport and exchange rate in the absence of DNA lesions. Third, the model faithfully describes MDC1 depletion kinetics at a region far from the lesion. Fourth, the model explains ATM exchange and recruitment kinetics, also allowing us to quantitatively predict the amount of ATM recruited at the DNA lesion. Our model is consistent with the data only if the diffusion rate of αATM is an order of magnitude slower than that of non-activated ATM (as was measured in our experiments) and similar to the MDC1 effective diffusion rate. A logical contributor to the slow diffusion rate of the activated ATM is its binding and unbinding from H2AX during phosphorylation. ATM activation is a critical step for γH2AX and MDC1 spread. It has been shown that ATM and DNA-PKs can phosphorylate H2AX, however only ATM promotes the spread of phosphorylation to large distances and high densities.[33] ATM binds to the MRN complex via the C-terminal domain of NBS1,[34] becomes activated, and phosphorylates hundreds of substrate proteins in addition to H2AX,[35] including multiple repair factors with diverse dynamics at DNA lesions.[8] It has been proposed that ATM auto-phosphorylation (at S367, S1893, S1981, S2996, and other potential sites) and/or disassociation of the ATM dimer triggers its activation.[36–38] The loss of auto-phosphorylation sites in human ATM reduces activation,[36,39] while mouse ATM with a mutation in the S1987 auto-phosphorylation site exhibits

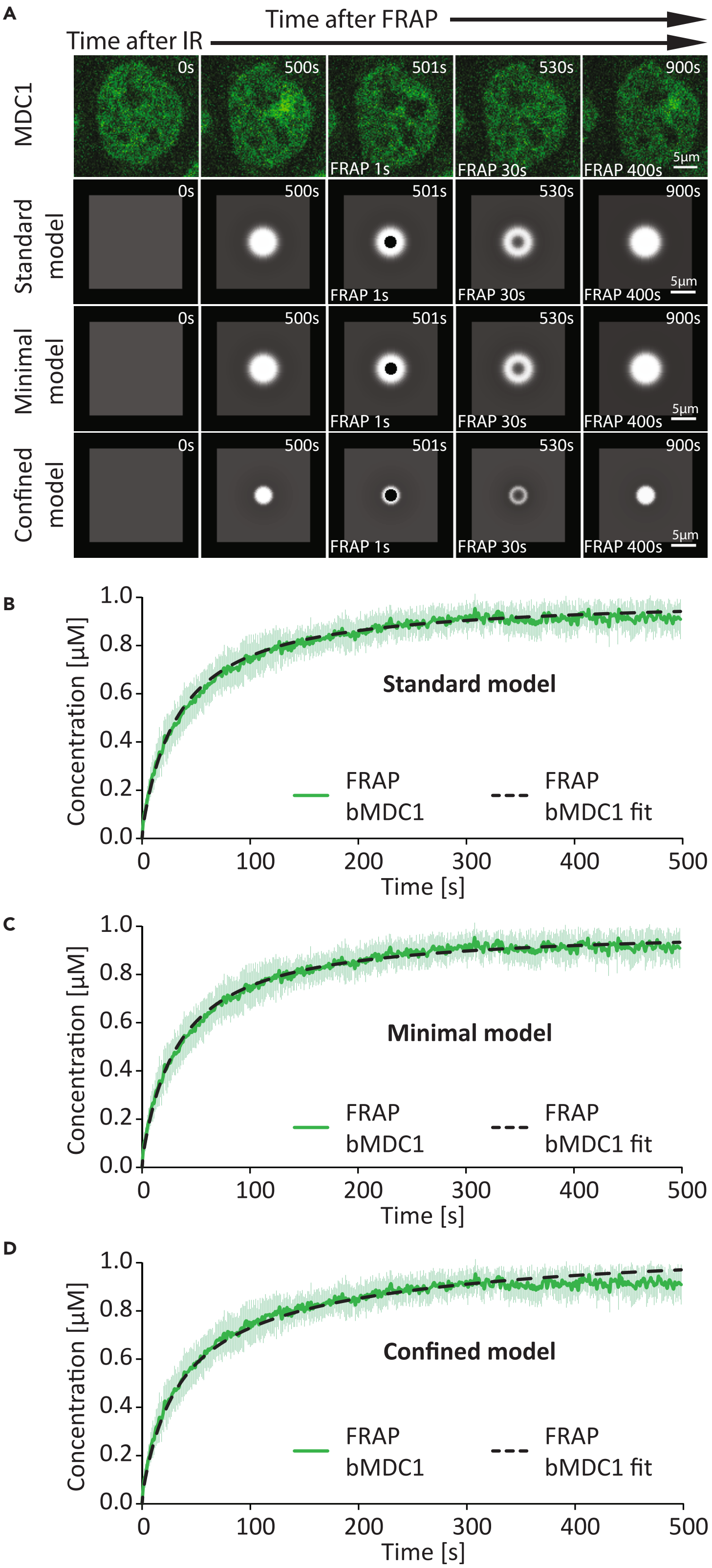
A
Time after FRAP
Time after IR
MDC1
Standard model
Minimal model
Confined model
0s
500s
501s
530s
900s
FRAP 1s
FRAP 30s
FRAP 400s
5μm
B
Standard model
C
Minimal model
D
Confined model
Concentration [μM]
Time [s]
0.0
0.2
0.4
0.6
0.8
1.0
0
100
200
300
400
500
FRAP bMDC1
FRAP bMDC1 fit

Figure 6. Comparison between the experimentally measured and predicted MDC1 dynamics at sites of complex DNA damage after FRAP

(A) Comparison between time-lapse microscopy images and images generated via simulation based on the models of MDC1 distribution at sites of complex DNA damage after FRAP. Scale bar: 5 μm.

(B) Graphical comparison between the experimentally measured dynamic MDC1 concentration (μM) at sites of complex DNA damage after FRAP ($N = 14$ foci) and that predicted based on the standard model. Data are presented as mean ± SD. FRAP bMDC1, measured concentration (μM) of MDC1 within the DNA damage site; FRAP bMDC1 fit, the best-fitting predicted concentration (μM) of MDC1 at the damage site, based on the standard model.

(C) Graphical comparison between the experimentally measured dynamic MDC1 concentration (μM) at sites of complex DNA damage after FRAP ($N = 14$ foci) and that predicted based on the minimal model. Data are presented as mean ± SD. FRAP bMDC1, measured concentration (μM) of MDC1 within the DNA damage site; FRAP bMDC1 fit, the best-fitting predicted concentration (μM) of MDC1 at the damage site, based on the minimal model.

(D) Graphical comparison between the experimentally measured dynamic MDC1 concentration at sites of complex DNA damage after FRAP ($N = 14$ foci) and that predicted based on the confined model. Data are presented as mean ± SD. FRAP bMDC1, measured concentration (μM) of MDC1 within the DNA damage site; FRAP bMDC1 fit, the best-fitting predicted concentration (μM) of MDC1 at the damage site, based on the confined model.

normal activation.[40–42] Further, several studies, including structural analyses,[43–46] suggest that ATM activation on DSBs can occur without the monomerization of the ATM dimer.[37] The αATM diffusion-based model of γH2AX/MDC1 spread proposed herein is consistent with the current mechanistic understanding of ATM activation.

It has been suggested that chromatin architecture plays an important role in the γH2AX spread, as topologically associated domains often coincide with phosphorylated H2AX regions.[19] In addition, it was shown that cohesin is recruited to the vicinity of a DSB, where it carries out loop extrusion, thus reshaping chromatin topology.[20] Locally activated ATM anchored at the loop boundary was also proposed to extensively phosphorylate H2AX by modifying the DNA that is actively extruded by cohesin in a unidirectional manner at the DSB.[20] However, cohesin depletion was shown to reduce H2AX phosphorylation by only 10%.[20] Herein, we provide two lines of evidence suggesting that cohesion-mediated loop extrusion is not the sole determinant of γH2AX spread at DNA damage sites. First, we show that cohesin loader NIPBL and cohesion subunit RAD21, which are required for loop extrusion, accumulate at a significantly slower rate than MDC1 recruitment and spread at micro-IR-induced complex DNA lesions. Second, we show that RAD21 degradation had no effect on γH2AX spread after micro-IR as well as after zeocin treatment. The fast rate of ATM exchange, which we measured at the DNA damage site, is also hard to reconcile with continuous loop extrusion-driven H2AX phosphorylation at the DSB. In contrast, our 3D model does recapitulate the experimental data. Several differences in experimental design may give rise to divergent results that are consistent with distinct models. First is the nature of the damage. Repetitive endonuclease-mediated cutting results in persistent DSB induction. While this approach enables the specific study of a single DSB, constant cutting at the same locus does not allow one to accurately follow the sequence of repair events through time. In this manner, one cannot conclusively determine whether loop extrusion is a cause or consequence of γH2AX/MDC1 spread. Meanwhile, micro-IR induces complex DNA lesions, i.e., chromatin at the damaged region incurs a variety of damage types, including single-strand breaks, DSBs, and base modifications.[8] Such complex lesions require the convergence and coordination of multiple repair pathways. Further, the multitude of insults may additionally alter chromatin topology. An advantage of this methodology is that damage induction occurs at a pre-defined timepoint and a confined nuclear region, which enables us to precisely follow sequential repair events. The over 200-s difference in recruitment half-time between MDC1 and RAD21 is clearly discernible through micro-IR combined with time-lapse live-cell microscopy. Such a difference cannot be detected through the sequencing-based study of repetitive DSB induction. Despite the distinct nature of complex DNA lesions relative to a single DSB, we still observe a clear spread of MDC1 at micro-IR regions. This indicates that the spread occurs, regardless of potential topological alterations in chromatin. We demonstrate that this spread cannot be explained by cohesin-mediated loop extrusion alone. Loop extrusion may play a role at a later stage of the DDR, as indicated by the kinetics of NIPBL and RAD21, which accumulate in parallel with BARD1, PAXIP, and 53BP1, shortly prior to the recruitment of RPA1 and RAD51, which are required for homologous recombination. Our measurements and mathematical models indicate that the spread can be easily explained by a 3D diffusion model of αATM. This model correctly predicts the measured recruitment kinetics, exchange rate, and diffusion of aATM and MDC1 as well as the MDC1 spread at complex DNA lesions.

In summary, we employed the introduced mathematical models to describe a central step of the cellular response to DNA damage. We are confident that our mathematical theory can be applied in the study of spatiotemporal fluctuations in protein concentrations in order to shed light on the molecular mechanisms underlying cellular processes.

Limitations of the study

The main limitation of the current work is rooted in the use of a limited number of cancer cell lines, namely, transgenic HeLa Kyoto and HCT116 cells. The majority of experiments were performed in HeLa Kyoto cells expressing GFP-tagged proteins of interest at near-endogenous levels, generated through BAC recombineering. It should be noted that the NIPBL transgene was of the mouse orthologue (mNIPBL). As discussed in our previous study, mNIPBL shared a high degree of homology with human NIPBL. Furthermore, the kinetics of the endogenous human cohesin subunit RAD21 (tagged with mClover via CRISPR-mediated knock-in) exhibited similar kinetics to those of cohesin loader mNIPBL, validating our measurements of cohesin/cohesin loader kinetics at the site of DNA damage. It should also be noted that multiple studies have reported the presence of cytoplasmic ATM in certain cell types.[47–50] However, we and others observe ATM localization exclusively within the nucleus of HeLa cells.[51] As a result, the models proposed herein do not consider the translocation of ATM between cytoplasm and nucleus in response to DNA damage.

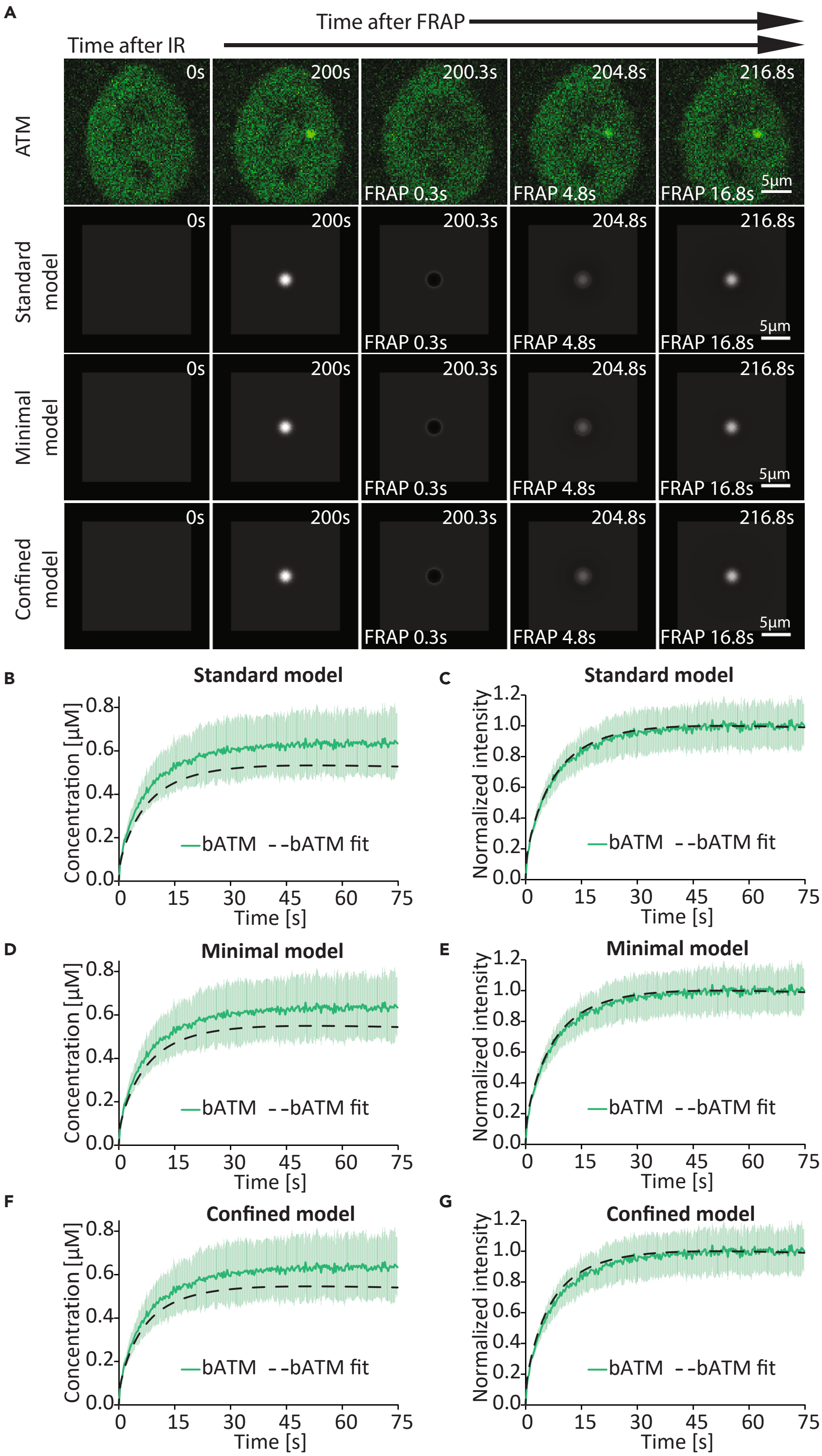
A
Time after FRAP
Time after IR
ATM
Standard model
Minimal model
Confined model
0s
200s
200.3s
204.8s
216.8s
FRAP 0.3s
FRAP 4.8s
FRAP 16.8s
5µm
B
Standard model
Concentration [µM]
0.0
0.2
0.4
0.6
0.8
0
15
30
45
60
75
Time [s]
bATM
bATM fit
C
Standard model
Normalized intensity
0.0
0.2
0.4
0.6
0.8
1.0
1.2
D
Minimal model
E
Minimal model
F
Confined model
G
Confined model

Figure 7. Comparison between the experimentally measured and predicted ATM dynamics at sites of complex DNA damage after FRAP

(A) Comparison between time-lapse microscopy images and images generated via simulation based on the models of ATM distribution at sites of complex DNA damage after FRAP. Scale bar: 5 μm.

(B) Graphical comparison between the experimentally measured dynamic ATM concentration at sites of complex DNA damage after FRAP (*N* = 16 foci) and that predicted based on the standard model. Data are presented as mean ± SD. FRAP bATM, measured concentration (μM) of ATM within the DNA damage site; FRAP bATM fit, the best-fitting predicted concentration (μM) of ATM at the damage site, based on the standard model.

(C) Graphical comparison between the normalized ATM kinetics at sites of complex DNA damage after FRAP (*N* = 16 foci) and those predicted based on the standard model. Data are presented as mean ± SD. FRAP bATM, measured concentration (μM) of ATM within the DNA damage site; FRAP bATM fit, the best-fitting predicted concentration (μM) of ATM at the damage site, based on the standard model.

(D) Graphical comparison between the experimentally measured dynamic ATM concentration at sites of complex DNA damage after FRAP (*N* = 16 foci) and that predicted based on the minimal model. Data are presented as mean ± SD. FRAP bATM, measured concentration (μM) of ATM within the DNA damage site; FRAP bATM fit, the best-fitting predicted concentration (μM) of ATM at the damage site, based on the minimal model.

(E) Graphical comparison between the normalized ATM kinetics at sites of complex DNA damage after FRAP (*N* = 16 foci) and those predicted based on the minimal model. Data are presented as mean ± SD. FRAP bATM, measured concentration (μM) of ATM within the DNA damage site; FRAP bATM fit, the best-fitting predicted concentration (μM) of ATM at the damage site, based on the minimal model.

(F) Graphical comparison between the experimentally measured dynamic ATM concentration at sites of complex DNA damage after FRAP (*N* = 16 foci) and those predicted based on the confined model. Data are presented as mean ± SD. FRAP bATM, measured concentration (μM) of ATM within the DNA damage site; FRAP bATM fit, the best-fitting predicted concentration (μM) of ATMat the damage site, based on the confined model.

(G) Graphical comparison between the normalized ATM kinetics at sites of complex DNA damage after FRAP (*N* = 16 foci) and those predicted based on the confined model. Data are presented as mean ± SD. FRAP bATM, measured concentration (μM) of ATM within the DNA damage site; FRAP bATM fit, the best-fitting predicted concentration (μM) of ATM at the damage site, based on the confined model.

RESOURCE AVAILABILITY

Lead contact

Further information and requests for resources and reagents should be directed to and will be fulfilled by the lead contact, Stoyno Stoynov, PhD (stoynov@bio21.bas.bg).

Materials availability

This study did not generate new unique reagents.

Data and code availability

- All data reported in this article will be shared by the lead contact upon request.
- All original code has been deposited at GitHub as well as Mendeley Data and is publicly available. DOIs are listed in the key resources table.
- Any additional information required to reanalyze the data reported in this article is available from the lead contact upon request.

ACKNOWLEDGMENTS

HCT-116-RAD21-mAID CMV-OsTIR1 cell line was a kind gift from Dr. Masato Kanemaki. G.D. and S.S.S. acknowledge the support from the Bulgarian NSF grant# KP-06-N21-9. K.B. B. was supported by the National Science Foundation, while working at the Foundation. Any opinion, finding and conclusions or recommendations expressed in this material are those of the authors and do not necessarily reflect the views of the National Science Foundation. G. P. was partially supported by the National Science Foundation. The authors acknowledge the support from the Sofia Euro-Bioimaging node of NRIR.

AUTHOR CONTRIBUTIONS

S.S.S, designed the experiments. G.D., R.A., and S.S.S. conducted the experiments. G.D., G.P., B.K., G.G., K.B.B., and S.S.S developed the mathematical model. A.A., R.S., S.U., and P.-B.K. analyzed the data. G.D. and B.K. wrote the numerical solution software with input from G.P. S.S.S., K.B.B., P.-B.K., and G.P. wrote the article. All authors commented on and edited the text.

DECLARATION OF INTERESTS

The authors declare no competing interests.

STAR★METHODS

Detailed methods are provided in the online version of this paper and include the following:

- KEY RESOURCES TABLE
- EXPERIMENTAL MODEL AND STUDY PARTICIPANT DETAILS
  - Cell lines
- METHOD DETAILS
  - Calculation of ATM1 and MDC1 nuclear concentrations
  - Micro-irradiation (IR) and image acquisition
  - Fluorescence recovery after photo bleaching (FRAP)
  - Micro-irradiation image and analysis
  - γH2AX immunofluorescence
  - Image analysis of FRAP and calculation of diffusion coefficients

  - ○ Mathematical modeling
- QUANTIFICATION AND STATISTICAL ANALYSIS

SUPPLEMENTAL INFORMATION

Supplemental information can be found online at https://doi.org/10.1016/j.isci.2024.110826.

Received: January 17, 2024
Revised: April 12, 2024
Accepted: August 22, 2024
Published: August 26, 2024

REFERENCES

1. Groelly, F.J., Fawkes, M., Dagg, R.A., Blackford, A.N., and Tarsounas, M. (2023). Targeting DNA damage response pathways in cancer. Nat. Rev. Cancer *23*, 78–94. https://doi.org/10.1038/s41568-022-00535-5.
2. Ashworth, A., and Lord, C.J. (2018). Synthetic lethal therapies for cancer: what's next after PARP inhibitors? Nat. Rev. Clin. Oncol. *15*, 564–576. https://doi.org/10.1038/s41571-018-0055-6.
3. Huang, R., and Zhou, P.K. (2021). DNA damage repair: historical perspectives, mechanistic pathways and clinical translation for targeted cancer therapy. Signal Transduct. Targeted Ther. *6*, 254. https://doi.org/10.1038/s41392-021-00648-7.
4. Sancar, A., Lindsey-Boltz, L.A., Unsal-Kaçmaz, K., and Linn, S. (2004). Molecular mechanisms of mammalian DNA repair and the DNA damage checkpoints. Annu. Rev. Biochem. *73*, 39–85. https://doi.org/10.1146/annurev.biochem.73.011303.073723.
5. Tubbs, A., and Nussenzweig, A. (2017). Endogenous DNA Damage as a Source of Genomic Instability in Cancer. Cell *168*, 644–656. https://doi.org/10.1016/j.cell.2017.01.002.
6. Aleksandrov, R., Hristova, R., Stoynov, S., and Gospodinov, A. (2020). The Chromatin Response to Double-Strand DNA Breaks and Their Repair. Cells *9*, 1853. https://doi.org/10.3390/cells9081853.
7. Polo, S.E., and Jackson, S.P. (2011). Dynamics of DNA damage response proteins at DNA breaks: a focus on protein modifications. Genes Dev. *25*, 409–433. https://doi.org/10.1101/gad.2021311.
8. Aleksandrov, R., Dotchev, A., Poser, I., Krastev, D., Georgiev, G., Panova, G., Babukov, Y., Danovski, G., Dyankova, T., Hubatsch, L., et al. (2018). Protein Dynamics in Complex DNA Lesions. Mol. Cell *69*, 1046–1061.e5. https://doi.org/10.1016/j.molcel.2018.02.016.
9. Babukov, Y., Aleksandrov, R., Ivanova, A., Atemin, A., and Stoynov, S. (2021). DNArepairK: An Interactive Database for Exploring the Impact of Anticancer Drugs onto the Dynamics of DNA Repair Proteins. Biomedicines *9*, 1238. https://doi.org/10.3390/biomedicines9091238.
10. Redon, C., Pilch, D., Rogakou, E., Sedelnikova, O., Newrock, K., and Bonner, W. (2002). Histone H2A variants H2AX and H2AZ. Curr. Opin. Genet. Dev. *12*, 162–169. https://doi.org/10.1016/s0959-437x(02)00282-4.
11. Rogakou, E.P., Boon, C., Redon, C., and Bonner, W.M. (1999). Megabase chromatin domains involved in DNA double-strand breaks in vivo. J. Cell Biol. *146*, 905–916. https://doi.org/10.1083/jcb.146.5.905.
12. Rogakou, E.P., Pilch, D.R., Orr, A.H., Ivanova, V.S., and Bonner, W.M. (1998). DNA double-stranded breaks induce histone H2AX phosphorylation on serine 139. J. Biol. Chem. *273*, 5858–5868. https://doi.org/10.1074/jbc.273.10.5858.
13. Sedelnikova, O.A., Pilch, D.R., Redon, C., and Bonner, W.M. (2003). Histone H2AX in DNA damage and repair. Cancer Biol. Ther. *2*, 233–235. https://doi.org/10.4161/cbt.2.3.373.
14. Goldberg, M., Stucki, M., Falck, J., D'Amours, D., Rahman, D., Pappin, D., Bartek, J., and Jackson, S.P. (2003). MDC1 is required for the intra-S-phase DNA damage checkpoint. Nature *421*, 952–956. https://doi.org/10.1038/nature01445.
15. Lou, Z., Chini, C.C.S., Minter-Dykhouse, K., and Chen, J. (2003). Mediator of DNA damage checkpoint protein 1 regulates BRCA1 localization and phosphorylation in DNA damage checkpoint control. J. Biol. Chem. *278*, 13599–13602. https://doi.org/10.1074/jbc.C300060200.
16. Lou, Z., Minter-Dykhouse, K., Franco, S., Gostissa, M., Rivera, M.A., Celeste, A., Manis, J.P., van Deursen, J., Nussenzweig, A., Paull, T.T., et al. (2006). MDC1 maintains genomic stability by participating in the amplification of ATM-dependent DNA damage signals. Mol. Cell *21*, 187–200. https://doi.org/10.1016/j.molcel.2005.11.025.
17. Stewart, G.S., Wang, B., Bignell, C.R., Taylor, A.M.R., and Elledge, S.J. (2003). MDC1 is a mediator of the mammalian DNA damage checkpoint. Nature *421*, 961–966. https://doi.org/10.1038/nature01446.
18. Natale, F., Rapp, A., Yu, W., Maiser, A., Harz, H., Scholl, A., Grulich, S., Anton, T., Hörl, D., Chen, W., et al. (2017). Identification of the elementary structural units of the DNA damage response. Nat. Commun. *8*, 15760. https://doi.org/10.1038/ncomms15760.
19. Collins, P.L., Purman, C., Porter, S.I., Nganga, V., Saini, A., Hayer, K.E., Gurewitz, G.L., Sleckman, B.P., Bednarski, J.J., Bassing, C.H., and Oltz, E.M. (2020). DNA double-strand breaks induce H2Ax phosphorylation domains in a contact-dependent manner. Nat. Commun. *11*, 3158. https://doi.org/10.1038/s41467-020-16926-x.
20. Arnould, C., Rocher, V., Finoux, A.L., Clouaire, T., Li, K., Zhou, F., Caron, P., Mangeot, P.E., Ricci, E.P., Mourad, R., et al. (2021). Loop extrusion as a mechanism for formation of DNA damage repair foci. Nature *590*, 660–665. https://doi.org/10.1038/s41586-021-03193-z.
21. Arnould, C., Rocher, V., Saur, F., Bader, A.S., Muzzopappa, F., Collins, S., Lesage, E., Le Bozec, B., Puget, N., Clouaire, T., et al. (2023). Chromatin compartmentalization regulates the response to DNA damage. Nature *623*, 183–192. https://doi.org/10.1038/s41586-023-06635-y.
22. Turing, A.M. (1952). The chemical basis of morphogenesis. Phil. Trans. Roy. Soc. Lond. B *237*, 37–72. https://doi.org/10.1098/rstb.1952.0012.
23. Poser, I., Sarov, M., Hutchins, J.R.A., Hériché, J.K., Toyoda, Y., Pozniakovsky, A., Weigl, D., Nitzsche, A., Hegemann, B., Bird, A.W., et al. (2008). BAC TransgeneOmics: a high-throughput method for exploration of protein function in mammals. Nat. Methods *5*, 409–415. https://doi.org/10.1038/nmeth.1199.
24. Zhang, Y., Buchholz, F., Muyrers, J.P., and Stewart, A.F. (1998). A new logic for DNA engineering using recombination in Escherichia coli. Nat. Genet. *20*, 123–128. https://doi.org/10.1038/2417.
25. Hein, M.Y., Hubner, N.C., Poser, I., Cox, J., Nagaraj, N., Toyoda, Y., Gak, I.A., Weisswange, I., Mansfeld, J., Buchholz, F., et al. (2015). A human interactome in three quantitative dimensions organized by stoichiometries and abundances. Cell *163*, 712–723. https://doi.org/10.1016/j.cell.2015.09.053.
26. Heyza, J.R., Mikhova, M., Bahl, A., Broadbent, D.G., and Schmidt, J.C. (2023). Systematic analysis of the molecular and biophysical properties of key DNA damage response factors. Elife *12*, e87086. https://doi.org/10.7554/eLife.87086.
27. Salguero, I., Belotserkovskaya, R., Coates, J., Sczaniecka-Clift, M., Demir, M., Jhujh, S., Wilson, M.D., and Jackson, S.P. (2019). MDC1 PST-repeat region promotes histone H2AX-independent chromatin association and DNA damage tolerance. Nat. Commun. *10*, 5191. https://doi.org/10.1038/s41467-019-12929-5.
28. Blackford, A.N., and Jackson, S.P. (2017). ATM, ATR, and DNA-PK: The Trinity at the Heart of the DNA Damage Response. Mol. Cell *66*, 801–817. https://doi.org/10.1016/j.molcel.2017.05.015.
29. Trakarnphornsombat, W., and Kimura, H. (2023). Live-cell tracking of gamma-H2AX kinetics reveals the distinct modes of ATM and DNA-PK in the immediate response to DNA damage. J. Cell Sci. *136*, jcs260698. https://doi.org/10.1242/jcs.260698.
30. Oka, Y., Suzuki, K., Yamauchi, M., Mitsutake, N., and Yamashita, S. (2011). Recruitment of the cohesin loading factor NIPBL to DNA double-strand breaks depends on MDC1, RNF168 and HP1gamma in human cells. Biochem. Biophys. Res. Commun. *411*, 762–767. https://doi.org/10.1016/j.bbrc.2011.07.021.

31. Natsume, T., Kiyomitsu, T., Saga, Y., and Kanemaki, M.T. (2016). Rapid Protein Depletion in Human Cells by Auxin-Inducible Degron Tagging with Short Homology Donors. Cell Rep. *15*, 210–218. https://doi.org/10.1016/j.celrep.2016.03.001.
32. Rao, S.S.P., Huang, S.C., Glenn St Hilaire, B., Engreitz, J.M., Perez, E.M., Kieffer-Kwon, K.R., Sanborn, A.L., Johnstone, S.E., Bascom, G.D., Bochkov, I.D., et al. (2017). Cohesin Loss Eliminates All Loop Domains. Cell *171*, 305–320.e24. https://doi.org/10.1016/j.cell.2017.09.026.
33. Savic, V., Yin, B., Maas, N.L., Bredemeyer, A.L., Carpenter, A.C., Helmink, B.A., Yang-Iott, K.S., Sleckman, B.P., and Bassing, C.H. (2009). Formation of dynamic gamma-H2AX domains along broken DNA strands is distinctly regulated by ATM and MDC1 and dependent upon H2AX densities in chromatin. Mol. Cell *34*, 298–310. https://doi.org/10.1016/j.molcel.2009.04.012.
34. Uziel, T., Lerenthal, Y., Moyal, L., Andegeko, Y., Mittelman, L., and Shiloh, Y. (2003). Requirement of the MRN complex for ATM activation by DNA damage. EMBO J. *22*, 5612–5621. https://doi.org/10.1093/emboj/cdg541.
35. Matsuoka, S., Ballif, B.A., Smogorzewska, A., McDonald, E.R., 3rd, Hurov, K.E., Luo, J., Bakalarski, C.E., Zhao, Z., Solimini, N., Lerenthal, Y., et al. (2007). ATM and ATR substrate analysis reveals extensive protein networks responsive to DNA damage. Science *316*, 1160–1166. https://doi.org/10.1126/science.1140321.
36. Bakkenist, C.J., and Kastan, M.B. (2003). DNA damage activates ATM through intermolecular autophosphorylation and dimer dissociation. Nature *421*, 499–506. https://doi.org/10.1038/nature01368.
37. Lee, J.H., and Paull, T.T. (2005). ATM activation by DNA double-strand breaks through the Mre11-Rad50-Nbs1 complex. Science *308*, 551–554. https://doi.org/10.1126/science.1108297.
38. Kozlov, S.V., Graham, M.E., Jakob, B., Tobias, F., Kijas, A.W., Tanuji, M., Chen, P., Robinson, P.J., Taucher-Scholz, G., Suzuki, K., et al. (2011). Autophosphorylation and ATM activation: additional sites add to the complexity. J. Biol. Chem. *286*, 9107–9119. https://doi.org/10.1074/jbc.M110.204065.
39. Kozlov, S., Gueven, N., Keating, K., Ramsay, J., and Lavin, M.F. (2003). ATP activates ataxia-telangiectasia mutated (ATM) in vitro. Importance of autophosphorylation. J. Biol. Chem. *278*, 9309–9317. https://doi.org/10.1074/jbc.m300003200.
40. Daniel, J.A., Pellegrini, M., Lee, J.H., Paull, T.T., Feigenbaum, L., and Nussenzweig, A. (2008). Multiple autophosphorylation sites are dispensable for murine ATM activation in vivo. J. Cell Biol. *183*, 777–783. https://doi.org/10.1083/jcb.200805154.
41. Pellegrini, M., Celeste, A., Difilippantonio, S., Guo, R., Wang, W., Feigenbaum, L., and Nussenzweig, A. (2006). Autophosphorylation at serine 1987 is dispensable for murine Atm activation in vivo. Nature *443*, 222–225. https://doi.org/10.1038/nature05112.
42. Menolfi, D., and Zha, S. (2020). ATM, ATR and DNA-PKcs kinases-the lessons from the mouse models: inhibition not equal deletion. Cell Biosci. *10*, 8. https://doi.org/10.1186/s13578-020-0376-x.
43. Baretic, D., Pollard, H.K., Fisher, D.I., Johnson, C.M., Santhanam, B., Truman, C.M., Kouba, T., Fersht, A.R., Phillips, C., and Williams, R.L. (2017). Structures of closed and open conformations of dimeric human ATM. Sci. Adv. *3*, e1700933. https://doi.org/10.1126/sciadv.1700933.
44. Xin, J., Xu, Z., Wang, X., Tian, Y., Zhang, Z., and Cai, G. (2019). Structural basis of allosteric regulation of Tel1/ATM kinase. Cell Res. *29*, 655–665. https://doi.org/10.1038/s41422-019-0176-1.
45. Yates, L.A., Williams, R.M., Hailemariam, S., Ayala, R., Burgers, P., and Zhang, X. (2020). Cryo-EM Structure of Nucleotide-Bound Tel1(ATM) Unravels the Molecular Basis of Inhibition and Structural Rationale for Disease-Associated Mutations. Structure *28*, 96–104.e3. https://doi.org/10.1016/j.str.2019.10.012.
46. Williams, R.M., Yates, L.A., and Zhang, X. (2020). Structures and regulations of ATM and ATR, master kinases in genome integrity. Curr. Opin. Struct. Biol. *61*, 98–105. https://doi.org/10.1016/j.sbi.2019.12.010.
47. Oka, A., and Takashima, S. (1998). Expression of the ataxia-telangiectasia gene (ATM) product in human cerebellar neurons during development. Neurosci. Lett. *252*, 195–198. https://doi.org/10.1016/s0304-3940(98)00576-x.
48. Hinz, M., Stilmann, M., Arslan, S.Ç., Khanna, K.K., Dittmar, G., and Scheidereit, C. (2010). A cytoplasmic ATM-TRAF6-cIAP1 module links nuclear DNA damage signaling to ubiquitin-mediated NF-kappaB activation. Mol. Cell *40*, 63–74. https://doi.org/10.1016/j.molcel.2010.09.008.
49. Yang, D.Q., Halaby, M.J., Li, Y., Hibma, J.C., and Burn, P. (2011). Cytoplasmic ATM protein kinase: an emerging therapeutic target for diabetes, cancer and neuronal degeneration. Drug Discov. Today *16*, 332–338. https://doi.org/10.1016/j.drudis.2011.02.001.
50. Berthel, E., Foray, N., and Ferlazzo, M.L. (2019). The Nucleoshuttling of the ATM Protein: A Unified Model to Describe the Individual Response to High- and Low-Dose of Radiation? Cancers *11*, 905. https://doi.org/10.3390/cancers11070905.
51. Li, J., Han, Y.R., Plummer, M.R., and Herrup, K. (2009). Cytoplasmic ATM in neurons modulates synaptic function. Curr. Biol. *19*, 2091–2096. https://doi.org/10.1016/j.cub.2009.10.039.
52. Danovski, G., Dyankova-Danovska, T., Stamatov, R., Aleksandrov, R., Kanev, P.B., and Stoynov, S. (2023). CellTool: An Open-Source Software Combining Bio-Image Analysis and Mathematical Modeling for the Study of DNA Repair Dynamics. Int. J. Mol. Sci. *24*, 16784. https://doi.org/10.3390/ijms242316784.
53. Schindelin, J., Arganda-Carreras, I., Frise, E., Kaynig, V., Longair, M., Pietzsch, T., Preibisch, S., Rueden, C., Saalfeld, S., Schmid, B., et al. (2012). Fiji: an open-source platform for biological-image analysis. Nat. Methods *9*, 676–682. https://doi.org/10.1038/nmeth.2019.
54. Schneider, C.A., Rasband, W.S., and Eliceiri, K.W. (2012). NIH Image to ImageJ: 25 years of image analysis. Nat. Methods *9*, 671–675. https://doi.org/10.1038/nmeth.2089.
55. Soumpasis, D.M. (1983). Theoretical analysis of fluorescence photobleaching recovery experiments. Biophys. J. *41*, 95–97. https://doi.org/10.1016/S0006-3495(83)84410-5.

STAR★METHODS

KEY RESOURCES TABLE

REAGENT or RESOURCE	SOURCE	IDENTIFIER
Antibodies		
Purified anti-H2A.X Phospho (Ser139) Antibody	Biolegend	Cat# 613401; RRID: AB_315794
Goat anti-Mouse IgG (H + L) Highly Cross-Adsorbed Secondary Antibody, Alexa Fluor™ 594	Thermo Fisher Scientific	Cat# A-11032; RRID: AB_2534091
Chemicals, peptides, and recombinant proteins		
3-indoleacetic acid	Sigma-Aldrich	Cat# I3750-5G-A
Zeocin	InvivoGen	Cat# ant-zn-1p
Ku-57788	Selleckchem	Cat# S2638
AZD6738	Selleckchem	Cat# S7693
FluoroBrite DMEM	Thermo Fisher Scientific	Cat# A1896701
GlutaMAX Supplement	Thermo Fisher Scientific	Cat# 35050061
Experimental models: Cell lines		
Human: HeLa Kyoto ATM-NFLAP cells	The Hyman Laboratory, MPI-CBG	2511
Human: HeLa Kyoto MDC1-LAP cells	The Hyman Laboratory, MPI-CBG	7720
Human: HeLa Kyoto mNIPBL-NFLAP cells	The Hyman Laboratory, MPI-CBG	5701
Human: HCT-116-RAD21-mAID-Clover CMV-OsTIR1	Dr. Masato Kanemaki[31]	NA
Software and algorithms		
CellTool	Danovski et al.[52]	https://dnarepair.bas.bg/software/CellTool/
BioModelSolver	This paper	https://data.mendeley.com/datasets/sspmr2js75/1 https://dnarepair.bas.bg/software/BioModelSolver https://github.com/GDanovski/BioModelSolver

EXPERIMENTAL MODEL AND STUDY PARTICIPANT DETAILS

Cell lines

We used HeLa Kyoto cell lines stably expressing ATM-NFLAP, MDC1-LAP, and mNIPBL-NFLAP fluorescently tagged proteins.[8,23] The HCT-116-RAD21-mAID-Clover CMV-OsTIR1 cell line, in which both RAD21 alleles are tagged with auxin-inducible degrons and an mClover reporter, was a kind gift from Dr. Masato Kanemaki.[31] All cell lines were cultured in Dulbecco's Modified Eagle Medium (DMEM) supplemented with 10% fetal bovine serum (FBS), 100 units/ml penicillin, and 100 μg/mL streptomycin at 37°C, 5% CO2. For micro-irradiation (IR) experiments and time-lapse imaging, we plated cells in MatTek glass bottom dishes (~20% confluence) and cultured them for 48 h. Prior to image acquisition, the medium was changed to FluoroBrite DMEM medium (Thermo Fisher Scientific), containing 10% FBS and 2 mM GlutaMAX Supplement (Thermo Fisher Scientific). For the combined ATR and DNA-PK inhibition experiment, cells were treated with 10 μM Ku-57788 (DNA-PKi) and 10 μM AZD6738 (ATRi) for 1 h prior to imaging.

METHOD DETAILS

Calculation of ATM1 and MDC1 nuclear concentrations

To determine the nuclear concentrations of MDC1 and ATM, we used the total numbers of MDC1 and ATM1 protein molecules per cell reported by Heine et al., that is, 45853 and 25928 protein molecules, respectively.[25] Considering that ATM and MDC1 are localized into the nucleus and that the average volume of HeLa Kyoto cell nuclei is 0.248 pL, we estimated that nuclear concentrations of MDC1 and ATM are 0.3028 μM and 0.155 μM, respectively.

Micro-irradiation (IR) and image acquisition

We performed micro-IR with an Andor Micropoint system, consisting of a 365nm dye laser pumped with a 337nm nitrogen laser at 3.5ns pulses with a pulse energy of 150 μJ. Micro-IR consisted of 10 pulses, with the 365nm dye laser output attenuated to 70% of the maximum. Cells were kept at 37°C and 5% CO2 during micro-IR experiments and image acquisition on an Andor Dragonfly 500 system equipped with a Nikon Eclipse Ti-E inverted microscope and a Nikon Perfect Focus System (PFS). We used a Nikon CFI Plan Apo 60x (NA 1.4) objective and an iXon888 EMCCD camera. Cells were imaged in three Z planes separated by 0.5 μm, at intervals of 0.5–5 s.

Fluorescence recovery after photo bleaching (FRAP)

To determine the exchange rate of DNA repair proteins at damage sites, we performed FRAP of foci after micro-IR. FRAP experiments were performed on an Andor Revolution System using a Nikon CFI Plan Apo VC 60x (NA 1.2) objective and an iXon897 EMCCD camera. After the concentration of proteins of interest in the irradiated cells reached a plateau, the micro-irradiated site was bleached (FRAP settings: 60μs dwell time, 20 repeats, 6% of the total energy of the 488nm laser −50mW).

Micro-irradiation image and analysis

To determine the kinetics of protein recruitment after micro-IR, we performed image analysis using our CellTool software,[52] as previously described. Three Z planes for every time point were combined using a maximum intensity projection, and the images from all time points were registered to compensate for cell movement. The average intensity (I) of both the region of protein recruitment and a nearby region were measured in order to calculate the difference between intensities of these two regions. Of note, IR-induced bleaching is the same at the site of DNA damage and the nearby region at time 0, showing that the bleached region is larger than the region of protein recruitment.

Therefore, the difference between the average intensities of the region of protein recruitment and the nearby region provides the average intensity of recruited proteins, which is compensated for bleaching during UV irradiation and image acquisition. This difference was multiplied by the protein recruitment area. Thereafter, the intensity of the post-IR frame was subtracted from the obtained intensity for every time point. Using these calculations, we obtained the total intensity of recruited proteins at DNA damage sites for a given time point.

To measure the spatial distribution of tagged proteins after micro-IR, the images were analyzed as follows. A region of interest encompassing the MDC1 signal spread around the damage site was cropped.[53,54] The cropped 2D images were converted to 1D via maximum intensity projection. The center of the focus was determined automatically as the pixel with the highest intensity, and, based on this, all the images were aligned in space. MDC1 does not homogenously spread outward of the damage focus due to the heterogeneous distribution of chromatin. Thus, we take the longest stretch of MDC1 spread in a given direction radiating from the focus. We are then able to follow the intensity of pixels away from the site of damage (i.e., pixels within the measured stretch) over time. To compare the observed spread to that predicted by different models, we mirror the intensity over time data, as if an analogous spread were happening in the opposite direction away from the focus.

γH2AX immunofluorescence

HCT-116-RAD21-mAID-Clover CMV-OsTIR1 cells were treated with or without 500uM auxin (3-indoleacetic acid, Sigma-Aldrich) for 1.5 h. Thereafter, auxin-treated or untreated cells were incubated with 100 μg/mL zeocin for 45 min. Micro-irradiated cells or cells treated with zeocin were fixed in 4% paraformaldehyde (PFA) for 10 min at room temperature (RT). PFA was washed with PBS three times for 5 min at RT. Then, cells were permeabilized with 0.25% Triton X-100 for 10 min at RT. Cells were again washed with PBS as described above, and blocking was performed with 1% bovine serum albumin (BSA) in PBST (PBS+0.1% Tween 20) for 30 min at RT. Primary mouse anti-γH2AX antibody (Biolegend, clone 2F3) was diluted 1:200 in 1% BSA in PBST. γH2AX detection with the primary antibody was carried out overnight at 4°C in a humidified chamber. Cells were washed with PBS and incubated with goat anti-mouse Alexa Fluor 594-conjugated secondary antibody at 1:1000 dilution in 1% BSA in PBS. Cells were incubated with the secondary antibody for 1 h at RT in the dark. Finally, cells were washed with PBS, and DAPI-containing Vectashield antifade mounting medium was added prior to imaging. The fixed cells were imaged using an Andor Dragonfly 500 or Andor Revolution System, with 10–12 z-planes acquired. Maximum intensity projection (MIP) was generated for the obtained images prior to analysis.

To assess γH2AX spread, we measured the fluorescence intensity profiles across the major axes of foci using the Plot Profile function in ImageJ.[53] We then aligned all measured foci along based on intensity peaks, measuring the average intensity at all points (pixels) along the whole profile. In addition to measuring the intensity profile, we determined the distribution of foci length. Foci length was defined as the distance between the two furthest pixels (of increased intensity) at the opposite ends of the major axis. The number of measured foci was 300. Data were analyzed via an unpaired t test. n.s. = not significant ($p = 0.0525$), significance level $p = 0.01$.

Image analysis of FRAP and calculation of diffusion coefficients

Image analysis of FRAP and calculation of diffusion coefficients was performed using CellTool. The average intensity in the photobleached region, in the whole cell nucleus, and in the background outside of the cell nucleus was measured. Those three values were used in order to normalize the data for acquisition bleach correction by applying the following formulas.[55]

Double normalization

$$I_{norm}^{double}(t) = \frac{Iref\_pre}{Iref(t) - Iback(t)} \cdot \frac{Ifrap(t) - Iback(t)}{Ifrap\_pre}$$

Where: $I_{norm}^{double}(t)$– double-normalized intensity; $Ifrap(t)$ – measured average intensity inside the bleached spot; $Iref(t)$ – measured average reference or whole studied compartment (cell, nucleus, etc.) intensity; $Iback(t)$ – measured average background intensity outside the cell; Subscript *_pre* means the averaging of intensity in the corresponding region of interest before bleach moment after subtraction of background intensity;

Full-scale normalization

$$I_{norm}^{full\ scale}(t) = \frac{I_{norm}^{double}(t) - I_{norm}^{double}(t_{bleach})}{1 - I_{norm}^{double}(t_{bleach})}$$

Where: $I_{norm}^{full\ scale}(t)$ - full-scale normalized intensity; $I_{norm}^{double}(t)$ - double-normalized intensity; $I_{norm}^{double}(t_{bleach})$- double-normalized intensity at the time of the bleach;

The following fit of the diffusion model for an oval region of interest to the acquired normalized FRAP data was performed as described in the CellTool manual. The used model can be briefly summarized by the following formula [Soumpasis]:

$$FRAP(t) = I \cdot e^{-\frac{w^2}{2Dt}} \left(I_0\left(\frac{w^2}{2Dt}\right) + I_1\left(\frac{w^2}{2Dt}\right) \right)$$

Where: $I_0(x), I_1(x),$ - modified Bessel functions. I – normalizing coefficient to account the incomplete recovery; D - diffusion coefficient [$\mu m^2 s^{-1}$]; w - the radius of bleach spot [μm]; t – time after the bleaching [s];

The diffusion coefficient of the free protein is obtained from the FRAP of the cells that were not micro-irradiated. The diffusion coefficient of the proteins at the binding site is calculated from the analysis of the FRAP of micro-irradiated cells.

Mathematical modeling

Reaction-diffusion equations

The reaction-diffusion equations for N concentrations A_i, Bi, and C_i are:

$$\frac{dA_i}{dt} = D_i \nabla^2 A_i + \sum_{i \neq j} B_{ij} A_j + C_j A_j$$

They can be treated as coupled initial-value problems over a grid of points covering the sample volume. For the case at hand, the focus site has cylindrical symmetry, so the grid consists of only a set of radial coordinates. At each time step, the diffusion term is evaluated across the grid, with the results combined with the B and C terms in the equation. To maintain stability of the diffusion terms, the time step Dt and the grid spacing Dr must satisfy the following constraint:

$$\frac{D_{max} \Delta t}{\Delta r^2} \ll 1$$

where D_{max} is the largest diffusion constant.

The stability and the convergence of the Laplacian were studied using both second- and fourth-order Laplacian finite difference expressions. The stability and the convergence of the time dependence were studied using both a first-order Euler and a fourth-order Runge-Kutta method. Using the relevant parameters for our models, Euler integration with second-order Laplacians were sufficient to provide stable, convergent results. The Laplacians were evaluated in parallel at each time step allowing the computation to be optimized on multi-core CPUs. The typical time step in the numerical solutions was 1 ms, and the grid spacing was 1 nm. The typical time of the numerical computations was around 1s.

The Nelder-Mead solver algorithm was used for automatic variation of the parameters of the models during fitting to the measured data.

We assume that the focus is in the center of a thick disc of radius R, and the concentration is symmetric in all directions, and depends only on the radius r to the center. The discrete Laplacian is calculated via

$$\nabla f(r) \approx \frac{1}{(dr)^2}(f(r - dr) + f(r + dr) - 2f(r)) + \frac{1}{2rdr}(f(r + dr) - f(r - dr))$$

Implementation of the reaction-diffusion equations for the models is presented in supplementary information. Simulation of ATM and MDC1 nuclear dynamics based on reaction-diffusion equations for each model was performed with BioModelSolver.

Image generation from the numerical solutions

The 2D images of the model were calculated based on the 1D model arrays using BioModelSolver. The distance of every pixel of the 2D image to the center of the image was calculated, and the corresponding intensity from the 1D model array was used. Additional normalization was applied to transform the intensity of the pixels to 8-bit integer values. The maximum calculated pixel intensity during the time-lapse was transformed to the maximum value of an 8-bit integer, and all other pixels were scaled with the same factor.

QUANTIFICATION AND STATISTICAL ANALYSIS

In order to determine whether there was a difference in the mean major axis length of γH2AX foci with versus without auxin-induced RAD21 degradation, we performed an unpaired t-test using JASP (Version 0.19.0). Three-hundred foci from each group were compared. The significance threshold was set at $p < 0.01$.